Electronic Supplementary Information (ESI) for

Constructing Robust Heterointerface for Carrier Viaduct via Interfacial Molecular Bridge Enables Efficient and Stable Inverted Perovskite Solar Cells

Huifen Xu,[1,2]† *Zheng Liang*,[1,2]† *Jiajiu Ye*,[1,3]* *Yong Zhang*,[5] *Zihan Wang*,[1,2] *Hui Zhang*,[1] *Changmao Wan*,[1,2] *Guangkun Xu*,[7] *Jie Zeng*,[5] *Baomin Xu*,[5] *Zhengguo Xiao*,[2,6] *Thomas Kirchartz*,[3,4] *and Xu Pan*[1]*

[1]Key Laboratory of Photovoltaic and Energy Conservation Material, Institute of Solid-State Physics, Hefei Institutes of Physical Science (HIPS), Chinese Academy of Sciences, Hefei 230031, China.

[2]University of Science and Technology of China (USTC), Hefei 230026, China.

[3]IEK5-Photovoltaics, Forschungszentrum Jülich, 52425 Jülich, Germany.

[4]Faculty of Engineering and CENIDE, University of Duisburg-Essen, 47057 Duisburg, Germany.

[5]Shenzhen Engineering Research and Development Center for Flexible Solar Cells, and Department of Materials Science and Engineering, Southern University of Science and Technology (SUSTech), Shenzhen 518055, China.

[6]Hefei National Laboratory for Physical Sciences at the Microscale and Department of Physics, University of Science and Technology of China (USTC), Hefei 230026, China.

[7]State Key Laboratory of Marine Resources Utilization in South China Sea, Hainan University, Haikou 570228, China.

*Correspondences: yejj@issp.ac.cn (J.Y.) and xpan@rntek.cas.cn (X.P.)

†These authors contributed equally to this work.

Contents

Note S1: The analysis for partitions of the efficiency loss and underlying physical mechanism for solar cells based on the Shockley Queisser model.[1]

The maximum output power (P_{max}) of perovskite solar cells (PSCs) is defined as, $P_{max} = J_{SC} \times V_{OC} \times FF$, the product of circuit-current density (J_{SC}), open-circuit voltage (V_{OC}), and fill factor (FF). Among those, FF generally depends on V_{OC} and the diversified physical parameters relating to the diode equation, such as resistive losses and ideality factor (n_{id}).[2] To quantitatively account for the efficiency losses, the departure of power conversion efficiency (PCE) from the ideal Shockley-Queisser (S-Q) model for the single-junction solar cells is described by five parameters highlighting different physical loss mechanisms,[3–6] as following equation.

$$\frac{PCE}{PCE^{SQ}} = \frac{J_{SC}}{J_{SQ}} \frac{V_{OC}}{V_{OC}^{rad}} \frac{V_{OC}^{rad}}{V_{OC}^{SQ}} \frac{FF_0(V_{OC})}{FF_0(V_{OC}^{SQ})} \frac{FF}{FF_0(V_{OC})} \quad (1)$$

where $\frac{J_{SC}}{J_{SC}^{SQ}}$ stands for photocurrent loss. Note that the maximum value of FF in solar cells is a function of the V_{OC}.[7,8] Thus, the FF losses in Equation (1) are described by two parts of $\frac{FF_0(V_{OC})}{FF_0(V_{OC}^{SQ})}$ and $\frac{FF}{FF_0(V_{OC})}$. Another two parts of $\frac{V_{OC}}{V_{OC}^{rad}}$ and $\frac{V_{OC}^{rad}}{V_{OC}^{SQ}}$ are dealing with V_{OC} loss. The corresponding physical mechanisms in PSCs of the losses are illustrated in **Table S1.** A detailed definition and discussion of the aforementioned parameters are available in ref. [3].

Table S1 The parameters used for the efficiency losses analysis and corresponding physical mechanism in PSCs.

Partition of efficiency losses	Parameters	Physical losses mechanisms
J_{SC} loss	$Fsc = \frac{J_{SC}}{J_{SC}^{SQ}}$	Photocurrent loss.
FF loss	$\frac{FF_0(V_{OC})}{FF_0(V_{OC}^{SQ})}$	FF loss owing to the loss in V_{OC}.
	$\frac{FF}{FF_0(V_{OC})}$	FF loses owning to the ideality factor and resistive

Voc loss	$\frac{V_{OC}}{V_{OC}^{rad}}$	V_{OC} loss owing to the non-radiative recombination.
	$\frac{V_{OC}^{rad}}{V_{OC}^{SQ}}$	The discrepancy between the actual absorption coefficient and the step assumed in the S-Q limit.

The value of $FF_0(V_{OC})$ without resistive losses can be calculated by the function as follows,

$$FF_0 = \frac{\frac{qV_{OC}}{n_{id}kT} - ln\left(\frac{qV_{OC}}{n_{id}kT} + 0.72\right)}{\frac{qV_{OC}}{n_{id}kT} + 1} \quad (2)$$

where q is the elementary charge, k is the Boltzmann constant, and T is the temperature of solar cells.[4] Equation (2) precisely describes the relationship between FF_0 without resistive losses and V_{OC}. Notably, for the calculation, the ideality factor of n_{id}=1 was assumed in this discussion. According to the S-Q detail balance, nonradiative open-circuit voltage loss (ΔV_{OC}^{nrad}),[9] is defined as the voltage loss between the radiative limit of the open-circuit voltage (V_{OC}^{rad}) and real measured V_{OC}, can be derived from the external luminescence quantum efficiency in logarithm (Q_e^{lum}).

$$\Delta V_{OC}^{nrad} = V_{OC}^{rad} - V_{OC} = -\frac{kT}{q} ln\left(Q_e^{lum}\right) \quad (3)$$

In this way, we can calculate the value of V_{OC}^{rad} from the equation (3), and thus obtain that of $FF_0\left(V_{OC}^{rad}\right)$.

In particular, we systematically visualized the partitioning of the efficiency losses among a range of typical reported PSCs both in the n-i-p and p-i-n configurations, according to ref. [3]. Therein, all statistical p-i-n PSCs employed PTAA as hole transport materials (HTMs). Based on the S-Q theory, **Fig. S1a** depicted the ratio of PCE with that of the S-Q theoretical limit value, and the corresponding photovoltaic paraterms were summarised in **Table S2**. The quantitative comparisons of specific loss contributions of them were depicted in **Fig. S1b**. Given considerable efforts have been invested in minimizing non-radiative recombination and photocurrent losses (yellow), the area of the green bars (V_{OC} losses) is no longer the largest in the case of high-

performing PSCs. In contrast, resistive losses, which reduce the FF losses (red) and account for the largest share in almost all PSCs in the n-i-p or p-i-n configurations, are the limiting factor. Resistive losses are associated with semiconductor electrodes and their selective contacts with perovskite. Especially, the HTMs substrate is the key for high-performing p-i-n devices.

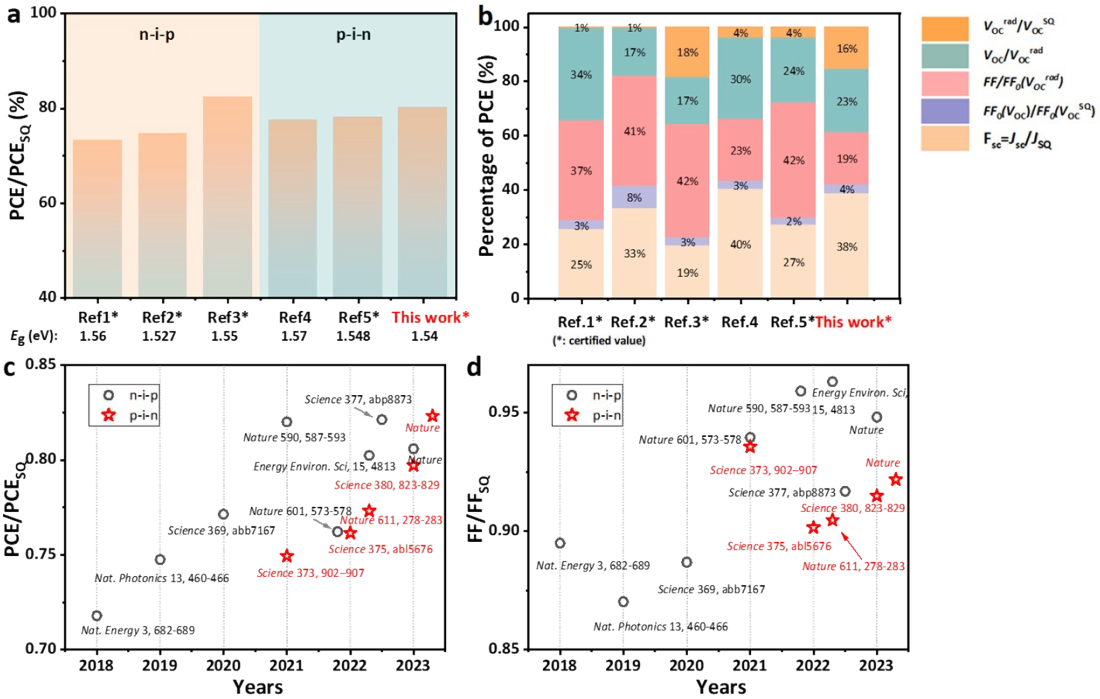

Fig. S1 Statistic diagrams for the photovoltaic parameters of the reported PSCs in conventional (n-i-p) and inverted (p-i-n) configurations. (**a**) The ratio of achieved PCE to S-Q theoretical value (PCE_{SQ}) of the reported PSCs in n-i-p and p-i-n configurations (*: certified values). (**b**) Overview of the partition of efficiency losses of the n-i-p and p-i-n PSCs (based on PTAA as HTM). While the specific partition of efficiency losses of other top-performing p-i-n PSCs cannot be calculated here due to lack of part key data, we thus reviewed the ratio of (**c**) PCE and (**d**) FF to the one in SQ limit.

Table S2 Overview of the photovoltaic parameters of the reported PSCs in the n-i-p and p-i-n configurations (Fig. S1; *: certified values).

References	V_{OC} (V)	J_{SC} (mA/cm^2)	FF (%)	PCE (%)	Configurations	E_g (eV)	V_{oc}^{SQ} (V)	FF/FF^{SQ}
Ref. 1[10]	1.144	22.67	79.6	22.67	n-i-p	1.56	1.273	0.88
Ref. 2*[11]	1.179	23.32	78.4	23.32	n-i-p	1.527	1.244	0.87
Ref. 3*[12]	1.18	26.3	82.60	25.60	n-i-p	1.55	1.264	0.91
Ref. 4[13]	1.18	24.13	85	23.7	p-i-n	1.57	1.282	0.94
Ref. 5*[14]	1.179	25.59	80.6	24.3	p-i-n	1.548	1.262	0.89
This work*	**1.148**	**25.32**	**85.6**	**24.9**	**p-i-n**	**1.54**	**1.253**	**0.95**

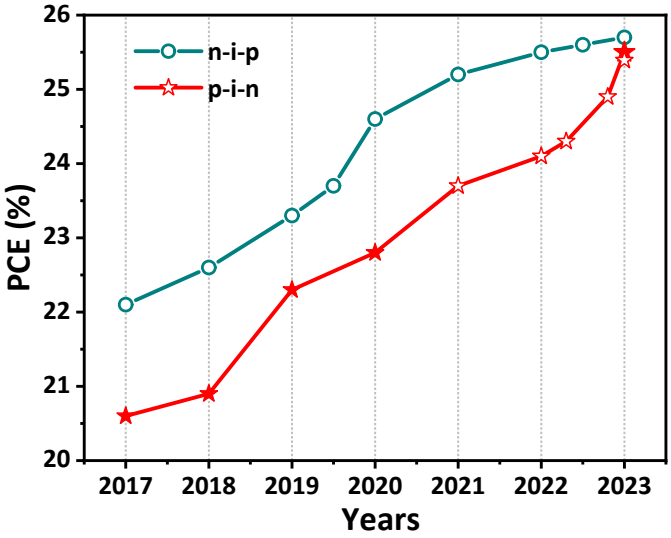

Fig. S2 Comparison of PCEs achieved by state-of-the-art cells in the n-i-p and p-i-n configurations.

The corresponding photovoltaic parameters of devices are presented at following Table S11.

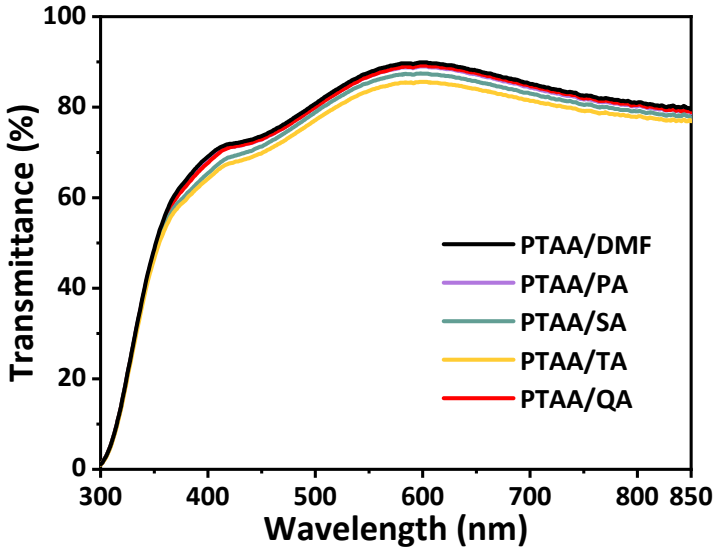

Fig. S3 Transmittance spectra of PTAA film without and with interfacial molecules post-treatment.

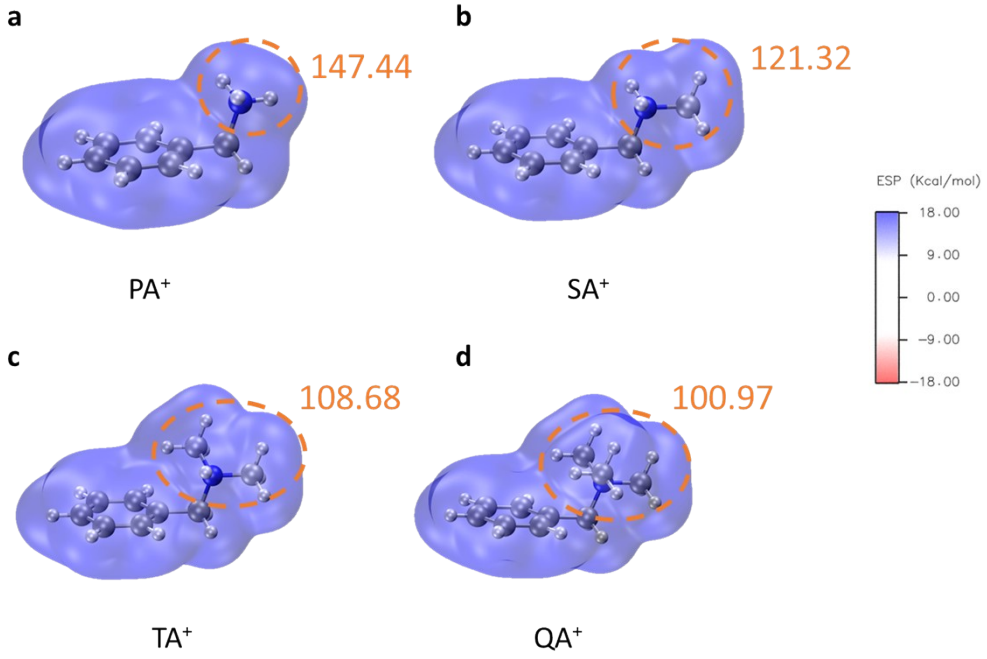

Fig. S4 The localized potential extremum for anchoring point N^+ of interfacial molecules by Gaussian calculation.

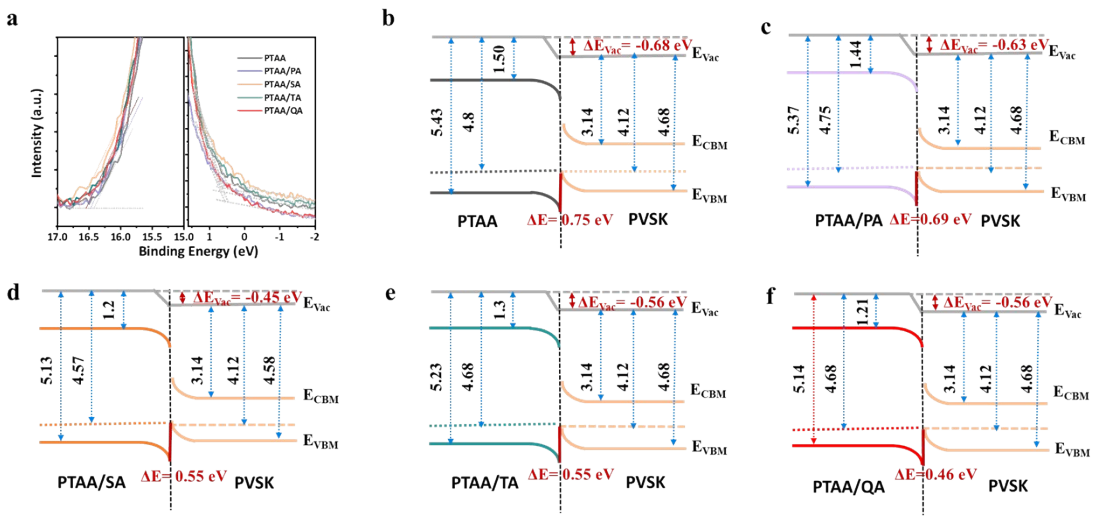

Fig. S5 Secondary electron cutoff and valence band obtained from ultraviolet photoelectron spectroscopy (UPS) spectra of (**a**) PTAA films. (**b-f**) Corresponding energy level alignment between perovskite and PTAA transport layers (E_F, Fermi energy level; E_{Vac}, vacuum level; E_{CBM}, conduction band minimum; E_{VBM}, valence band maximum; $\Delta E_{Vac}=E_{Vac}^{PVSK}- E_{Vac}^{PTAA}$; ΔE, energy barrier).[15]

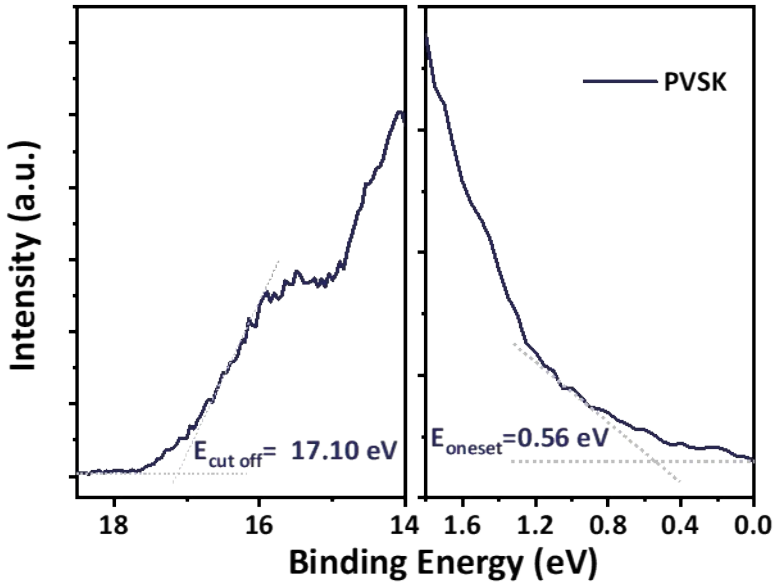

Fig. S6 Secondary electron cutoff and valence band obtained from ultraviolet photoelectron spectroscopy (UPS) spectra of perovskite films

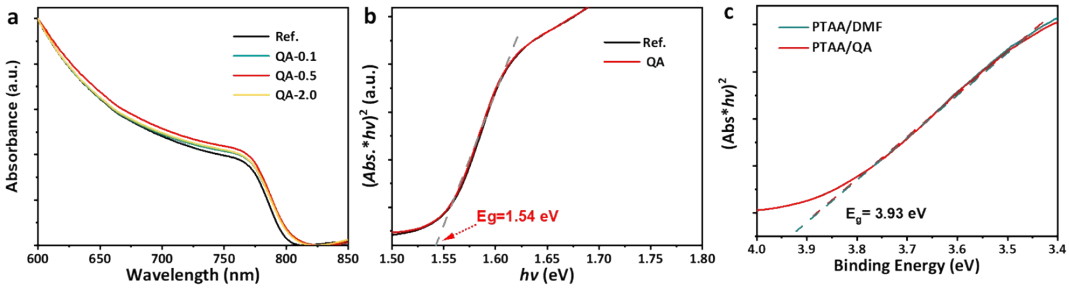

Fig. S7 (**a**) Ultraviolet-visible (UV-vis) absorption and (**b**) corresponding Tauc plots of reference and QA-based perovskite films deposited on PTAA substrates. (**c**) Tauc plots of PTAA/DMF, and PTAA/QA films.

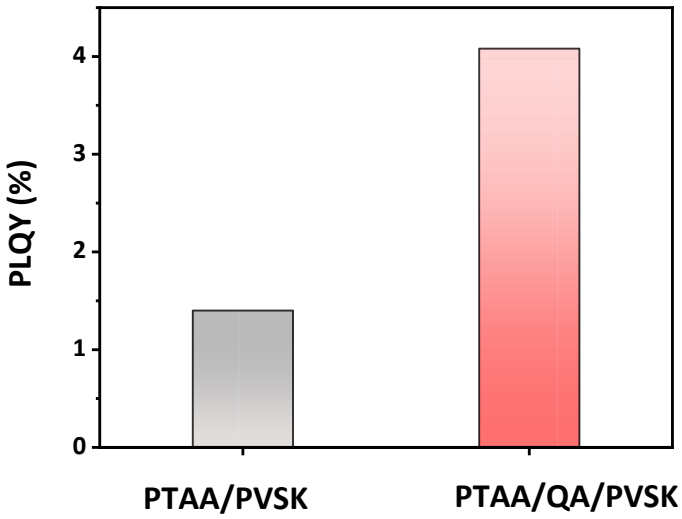

Fig. S8 The photoluminescence quantum yield (PLQY) of PTAA/PVSK and PTAA/QA/PVSK stack devices.

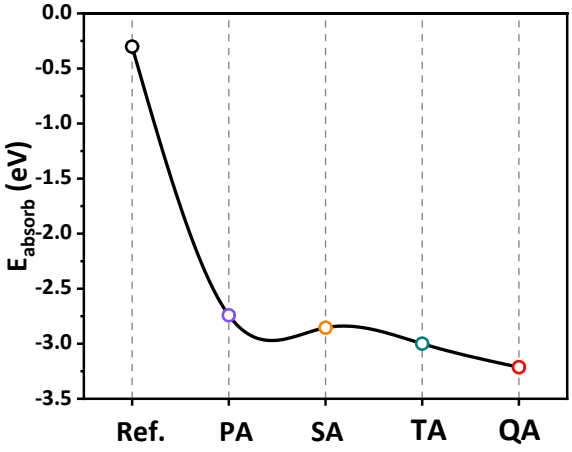

Fig. S9 Statistical diagram for adsorption energy of devices with interfacial molecules treatment by DFT calculation.

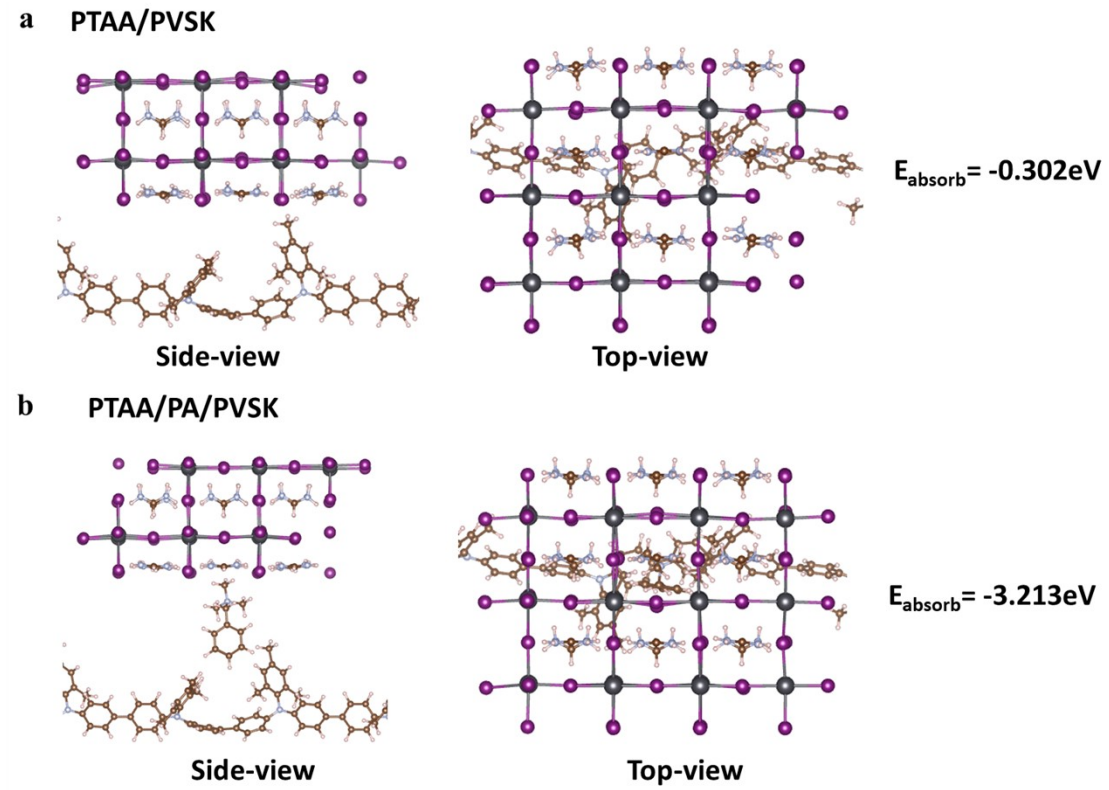

Fig. S10 The absorption energy of (**a**) PTAA/PVSK and (**b**) PTAA/QA/PVSK heterojunction under the side and top views, respectively.

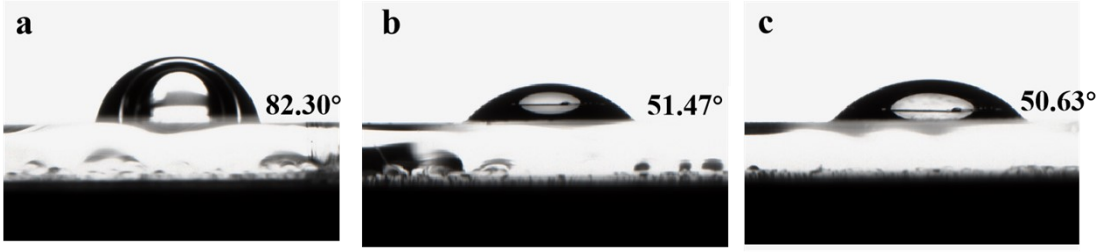

Fig. S11 Water contact angle images of (**a**) PTAA, (**b**) PTAA/DMF, and (**c**) PTAA/QA films.

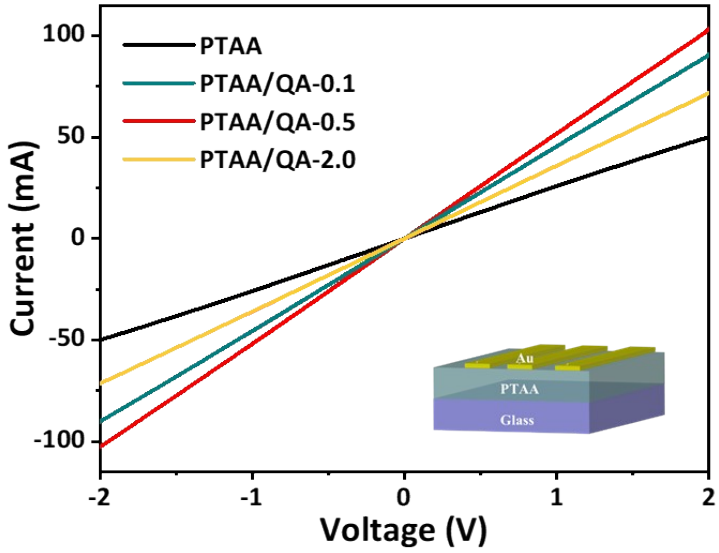

Fig. S12 The current-voltage curves of PTAA without and with QA treatment. The different concentrations of QA in 0.1, 0.5, and 2.0 mg mL^{-1} are labeled as QA-0.1, QA-0.5, and QA-2.0, respectively.

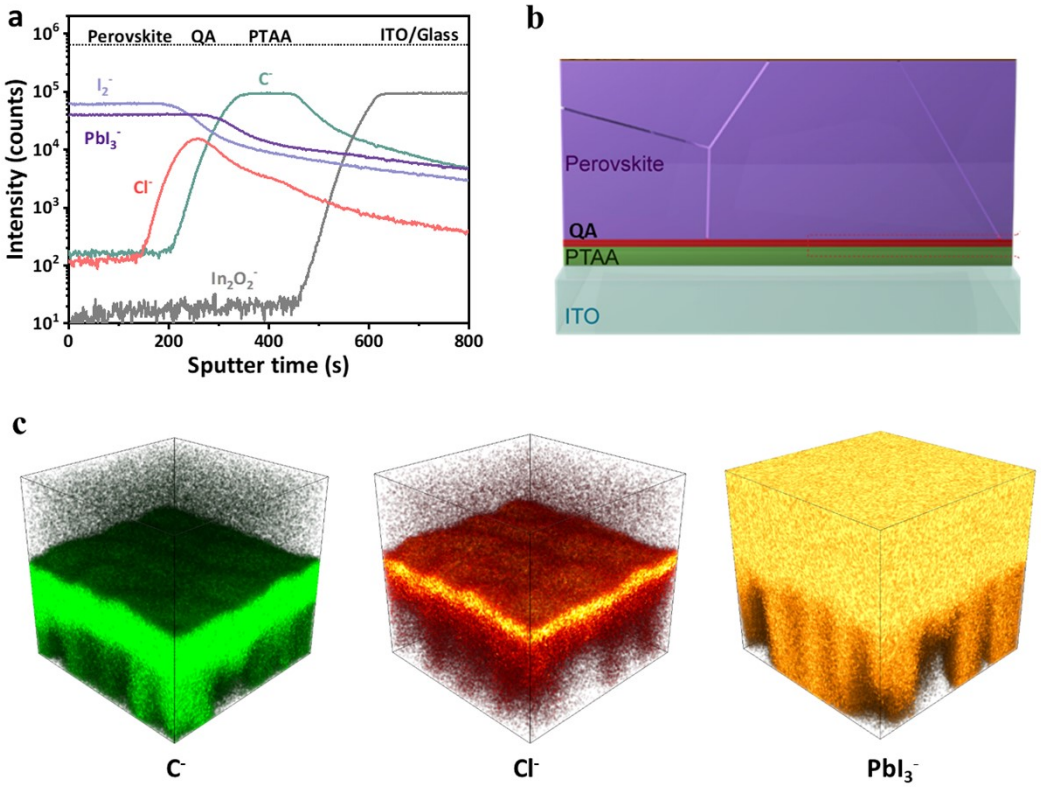

Fig. S13 (**a**) Time-of-flight secondary ion mass spectroscopy (ToF-SIMS) profiles. (**b**) The structure of the half-stack devices. (**c**) corresponding 3D distribution picture of the half-stack devices of ITO/PTAA/QA/Perovskite.

Note: The signal of Cl^- originates from QA molecule, while the PbI_3^-, C^-, and $In_2O_2^-$ ions are assigned to the perovskite layer, PTAA layer and ITO substrate, respectively. Noteworthy is that the perovskite precursor of the sample did not use MACl additive to eliminate interference of Cl^- ion for QA. As shown in Fig. S13a, Cl^- is distributed at the interface between PTAA and perovskite layer, indicating the presence of QA at the buried interface of PTAA/perovskite.

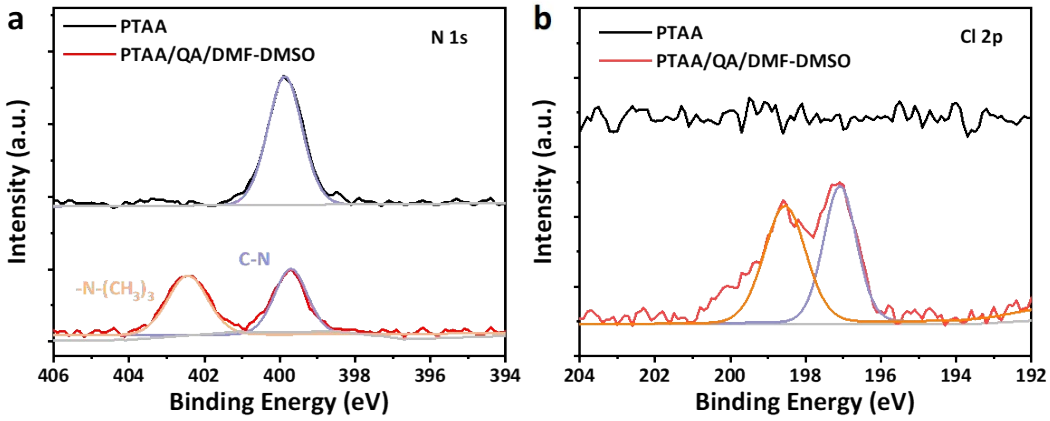

Fig. S14 X-ray photoelectron spectroscopy (XPS) spectra for (**a**) N 1s and (**b**) Cl 2p core-levels of pure PTAA and PTAA/QA films after washed by the mixture solution of DMF/DMSO (v: v=4:1).

Note: To confirm the existence of QA at the interface, we compared the Cl 2p core level of clean PTAA and that washed by a mixture solution of DMF/DMSO (v/v= 4/1, same as perovskite solution). The visible new peaks at 197.1 and 198.5 eV of the washed PTAA/QA film indicate that QA remained residuals at the interface rather than washed away by perovskite precursors. Additionally, the new peak appearing in N 1s core level of PTAA/QA film further confirms the existence of QA.

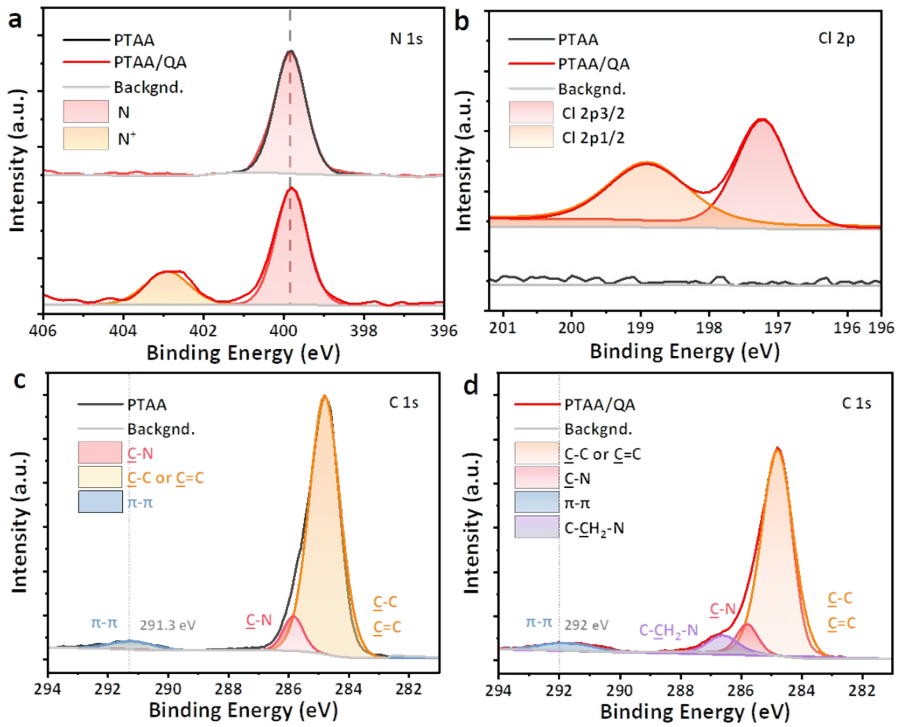

Fig. S15 X-ray photoelectron spectroscopy (XPS) spectra for (**a**) N 1s, (**b**) Cl 2p, and (**c-d**) C 1s core-levels of PTAA and PTAA/QA films.

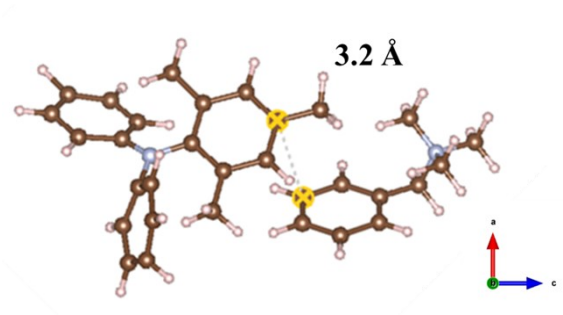

Fig. S16 (**a**) The distance between the corresponding carbon atoms in the phenyl group of PTAA and QA molecule is calculated to be ~3.2 Å.

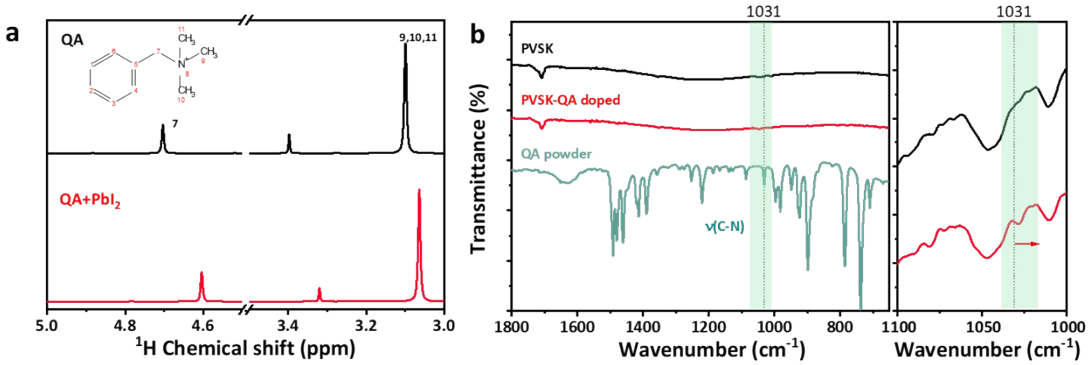

Fig. S17 (**a**) Liquid-state 1H NMR spectra of QA with or without mixing with PbI_2 in DMSO-d6. (**b**) FTIR spectra of pure PbI_2 powder, perovskite film doped without and with QA.

Note: We carried out nuclear magnetic resonance (NMR) and Fourier-transform infrared spectroscopy (FTIR) measurements to study how QA interacts with PbI_2. The obvious shift of the ^{1}H NMR peaks in QA+PbI_2 indicates the interaction between QA and PbI_2. As shown in Fig. S17a, C-N stretching peak at 1031 cm^{-1} from QA could be distinguished readily from reference perovskite and QA-doped perovskite. Meanwhile, the C-N stretching peak in QA-doped perovskite exhibited a slight blue-shift from 1031 to 1028.5 cm^{-1}, indicating the presence of interaction between QA and perovskite.

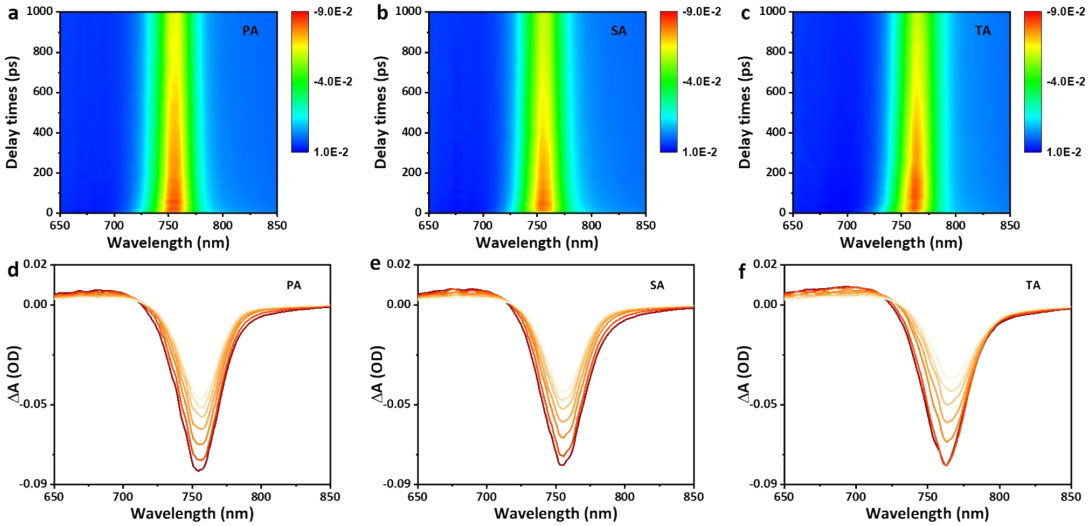

Fig. S18 (**a-b**) Transient absorption spectroscopy (TA) spectra of perovskite films deposited on PTAA with interfacial molecules treatment: PTAA/PA/PVSK**,** (**b**) PTAA/SA/PVSK**,** (**c**) PTAA/TA/PVSK. (**d-f**) Corresponding TA spectra at different decay times of heterojunction.

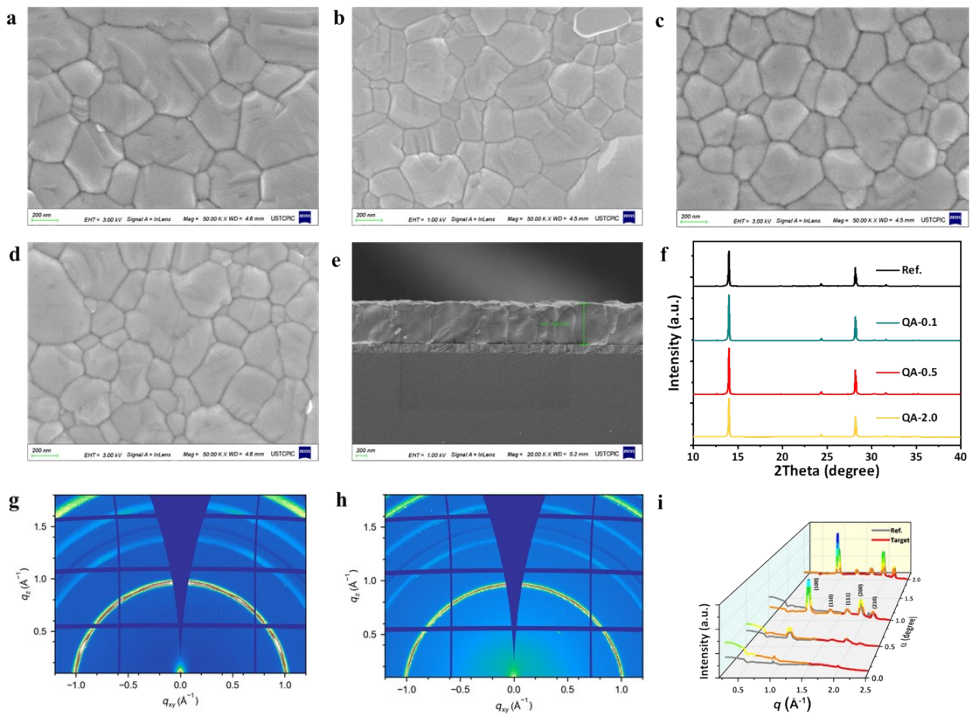

Fig. S19 Top-view scanning electron microscopy (SEM) images of (**a**) reference and target perovskite films deposited on PTAA films with different concentrations of QA, (**b**) 0.1 mg/mL, (**c**) 0.5 mg/mL, and (**d**) 2.0 mg/mL. **(e)** Cross-view SEM image of target perovskite films, where the thickness of the perovskite absorber was ~798.3 nm. **(f)** X-ray diffraction (XRD) patterns of the perovskite with QA treatment in different concentrations. **g-i,** Grazing-incidence wide-angle X-ray scattering (GIWAX) patterns of (**g**) reference and (**h**) target perovskite films deposited on PTAA substrate. (**i**) The corresponding XRD pattern in the different scattering degrees (χ = 0.2°, 0.5°, 1.0°, 1.5°, 2.0°).

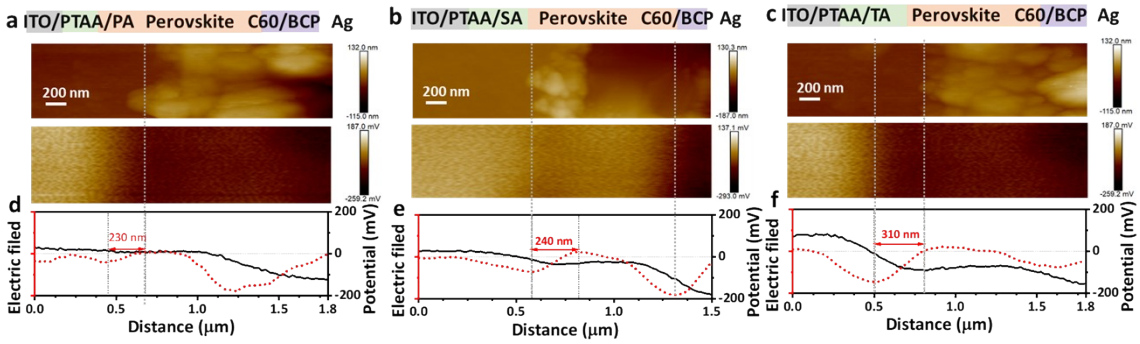

Fig. S20 Cross-sectional atomic force microscopy (AFM), corresponding Kelvin probe force microscopy (KPFM) images, and corresponding potential profiles (black lines) and electric filed (red lines) of the whole (**a**) PA-, (**b**) SA-, and (**c**) TA-based devices**.**

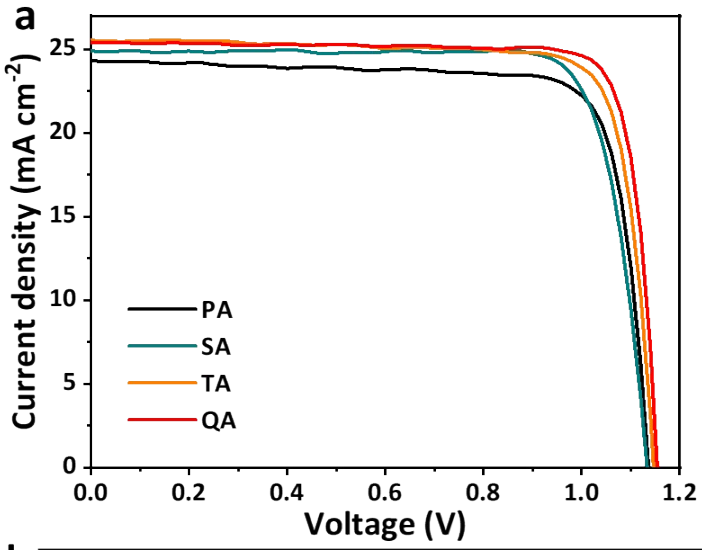

b

Devices	*V*oc (V)	*J*sc (mA cm^{-2})	FF (%)	PCE (%)
PA	1.13	24.32	80.36	22.39
SA	1.13	24.89	81.65	23.24
TA	1.14	25.53	81.63	24.09
QA	1.15	25.42	84.53	24.98

Fig. S21 (**a**) The current density-voltage (*J*-*V*) curves and (**b**) the corresponding photovoltaic parameters of the devices with different interfacial molecules treatment.

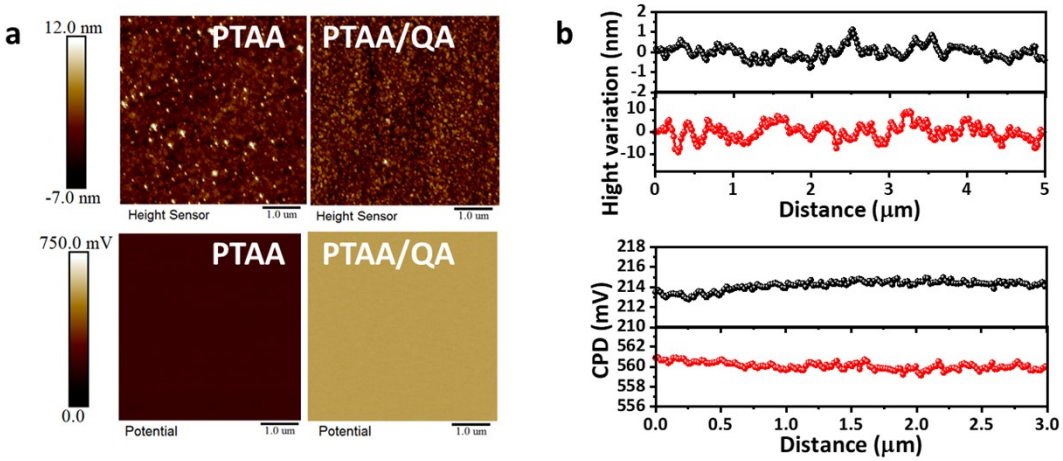

Fig. S22 (**a**) AFM (top) and KPFM surface potential images (bottom) of PTAA films without and with QA. (**b**) The corresponding height (top) and contact potential difference (CPD) variations (bottom) from KPFM measurement.

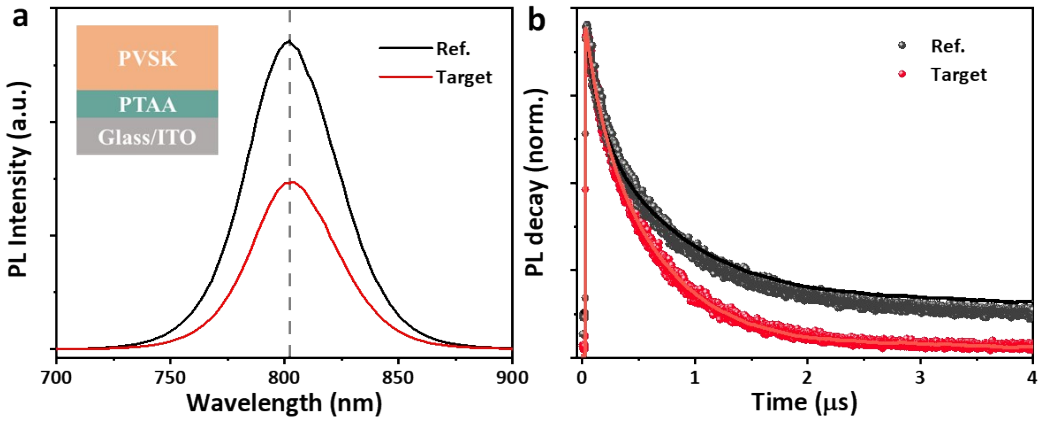

Fig. S23 (**a**) Stead-state photoluminescence (PL) and (**b**) time-resolved photoluminescence (TRPL) spectra of films with the structure of ITO/PTAA/QA/perovskite. Stead-state PL used an excitation light of 480 nm.

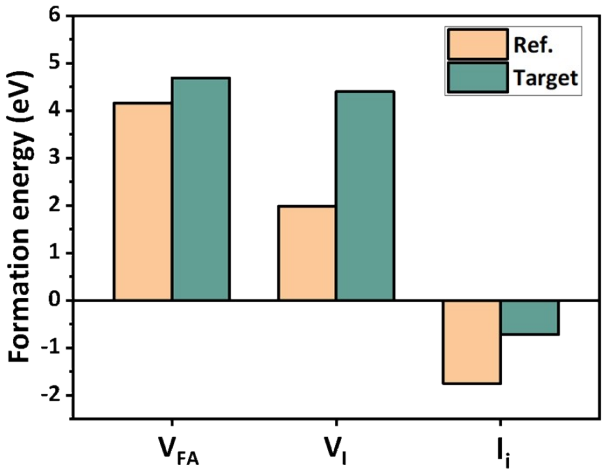

Fig. S24 The calculated formation energy of FA vacancies (V_{FA}), I-vacancies (V_I), and I interstitials (I_i) at the FAI-terminated surface.

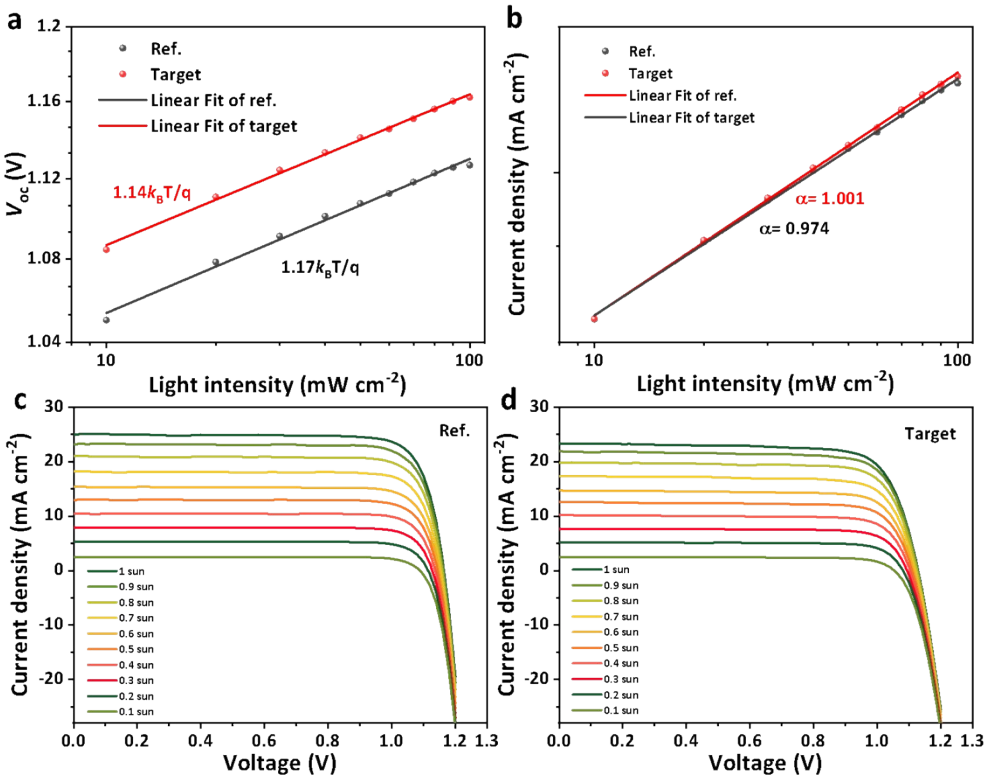

Fig. S25 The dependence of (**a**) V_{OC} and (**b**) J_{SC} on the light intensity of solar cells with corresponding *J-V* curves (**c-d**) under different illustrations.

Note: The slope of the V_{OC} concerning the light intensity curve is related to the ideality factor (n), where n of 1 and 2 is respectively associated with the full radiative recombination and non-radiative Shockley-Read-Hall recombination[16]. The smaller deviation between the slope (α) value of the J_{SC} on the light intensity curves and one indicates that more charge carriers of perovskite absorber are collected by the transport layers.

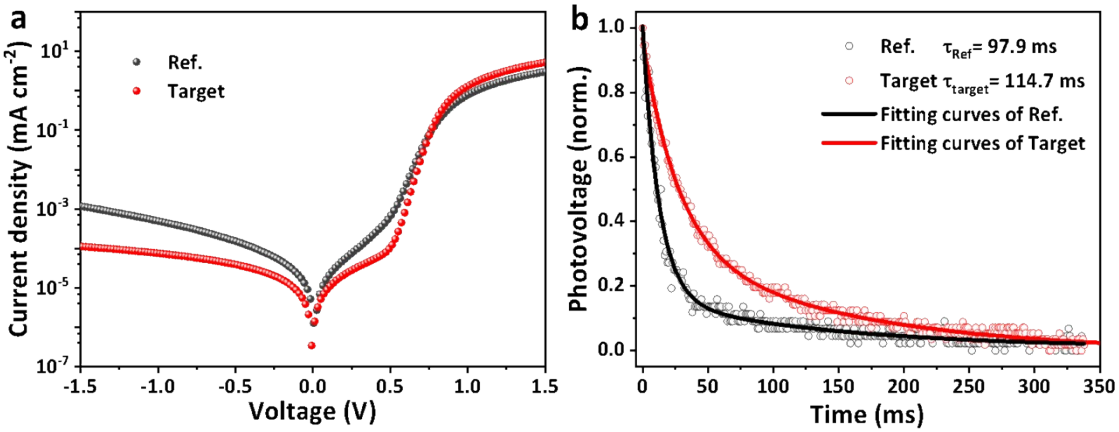

Fig. S26 (**a**) Dark *J-V* curves of reference and target devices. (**b**) Normalized transient photovoltaic (TPV) decay kinetic for reference and target solar cells.

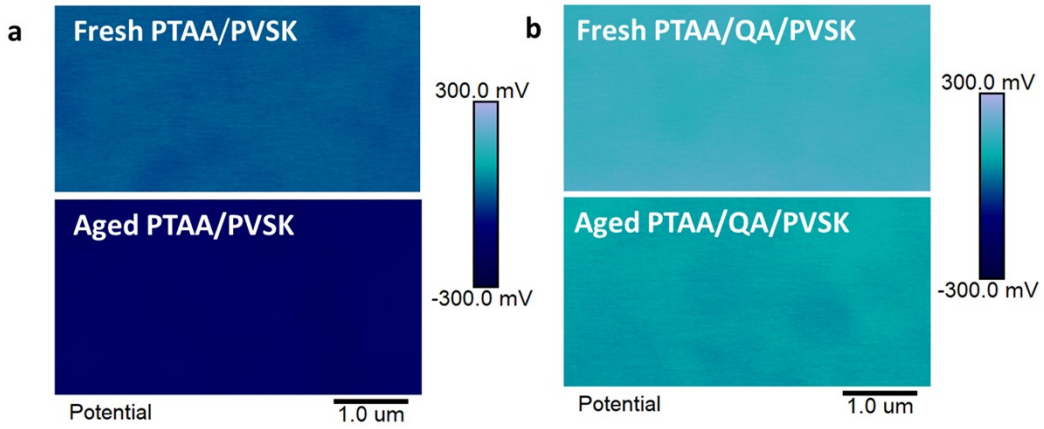

Fig. S27 Surface potential mapping images of (**a**) PTAA/PVSK without and (**b**) with QA treatment before (top) and after (bottom) exposure to light for 300 hours.

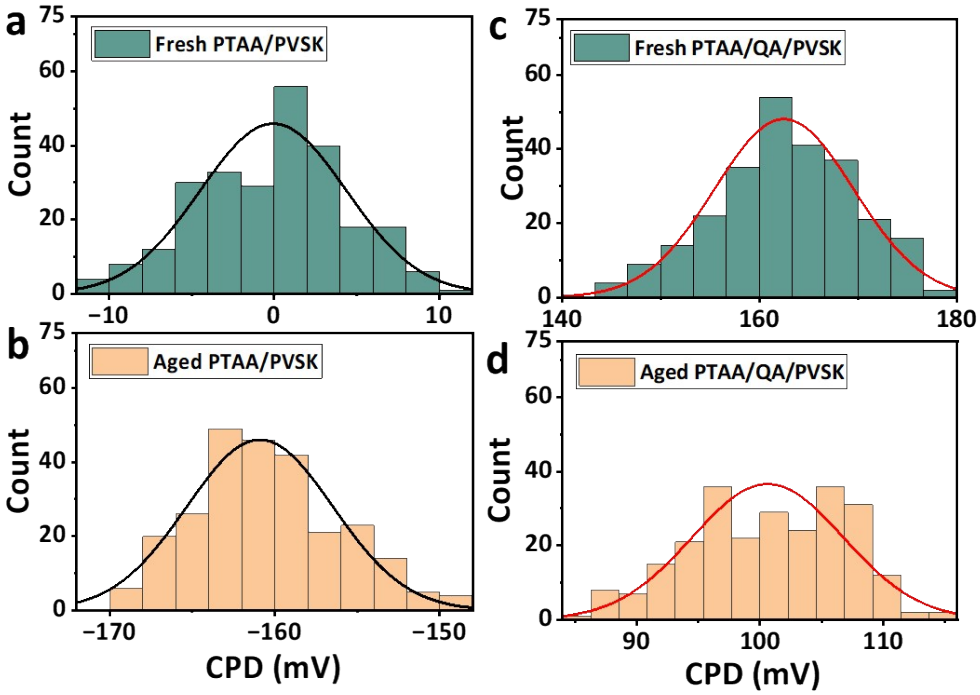

Fig. S28 Schematic of CPD value distribution and corresponding Gauss fitting curves for PTAA/PVSK and PTAA/QA/PVSK heterojunctions (**a, c**) before and (**b, d**) after aging, respectively.

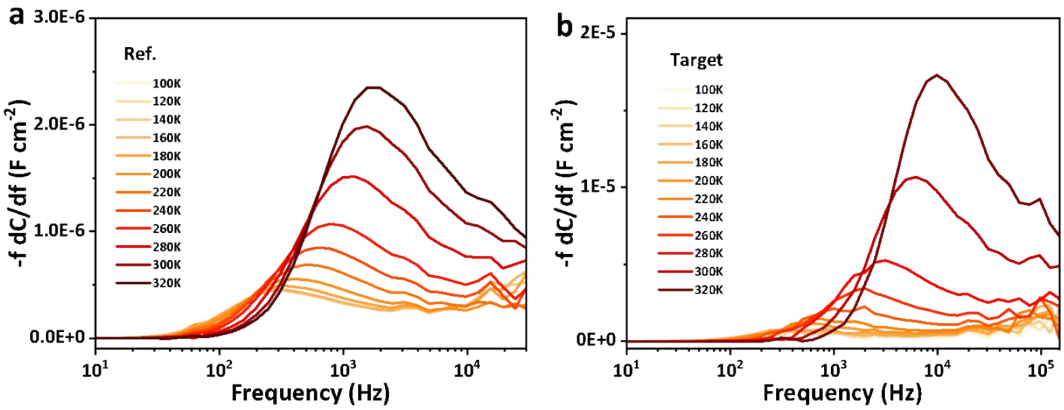

Fig. S29 Corresponding $-\omega dC/d\omega$ versus ω spectra of the capacitance-frequency-temperature (C-f-T) spectra of (**a**) the reference and (**b**) target devices measured from 100 to 320 K with a step of 20 K.

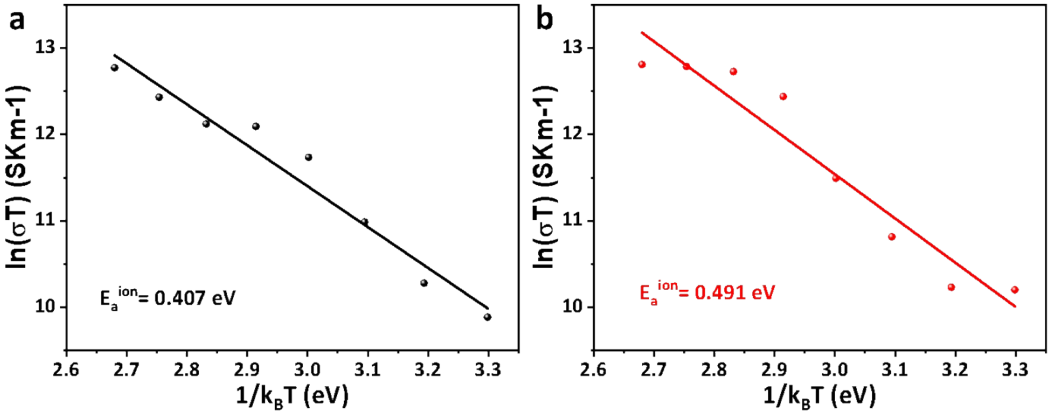

Fig. S30 The temperature-dependent conductivity of (**a**) reference and (**b**) target devices. The study of ion migration based on the Nernst-Einstein relationship[17], $\sigma T = \sigma_0 exp(-E_a/k_B T)$, where σ is ionic conductivity, T is temperature, k_B is Boltzmann constant and E_a is the ion migration activation energy derived from the slope of $ln(\sigma T)$ versus $1/T$.

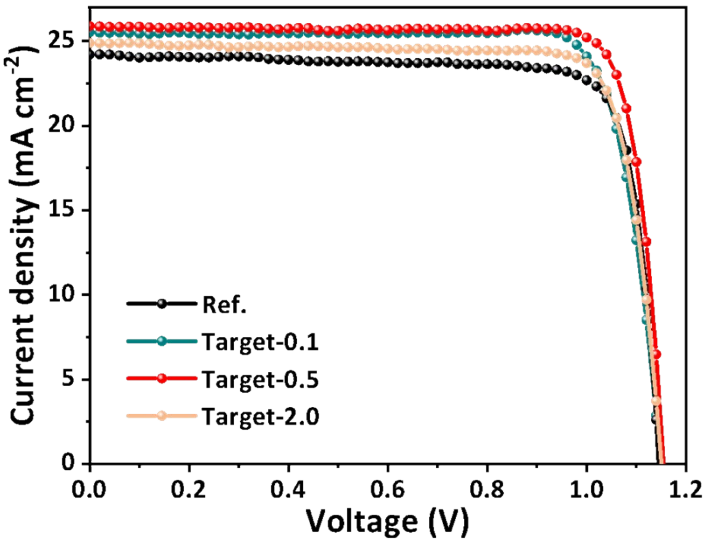

Fig. S31 *J-V* curves of the devices with QA treatment in different concentrations (0.1, 0.5, and 2.0 mg mL^{-1} of QA-based devices are labeled as target-0.1, target-0.5, and target-2.0, respectively).

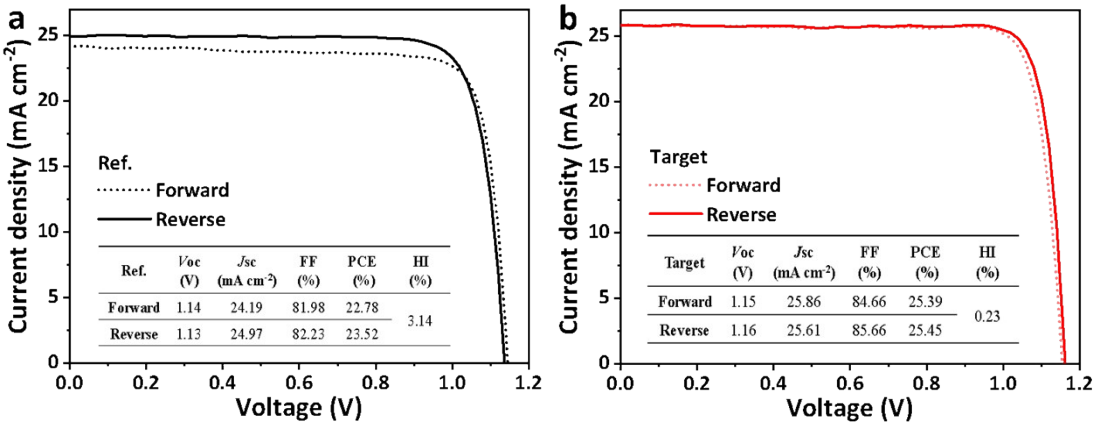

Fig. S32 *J-V* curves of the champion devices (**a**) without and (**b**) with QA under different scanning directions. The gap between the forward and reverse *J-V* curves can gauge the severity degree of hysteresis, quantitatively described by hysteresis index (HI), $HI = \frac{PCE_{RS} - PCE_{FS}}{PCE_{RS}}$.

170021162056

中国认可
检测
TESTING
CNAS L2338

TEST REPORT

Report No：PWQC-WT-P22102821-1R

Sample Name : Photovoltaic cell

Client : Hefei Institutes of Physical Science, CAS

Client Address : No. 350, Shushanhu Rd, Hefei, Anhui

Type of Project : Consignation

业务专用章

PHOTOVOLTAIC AND WIND POWER SYSTEMS QUALITY TEST CENTER, IEE, CHINESE ACADEMY OF SCIENCES

November 16, 2022

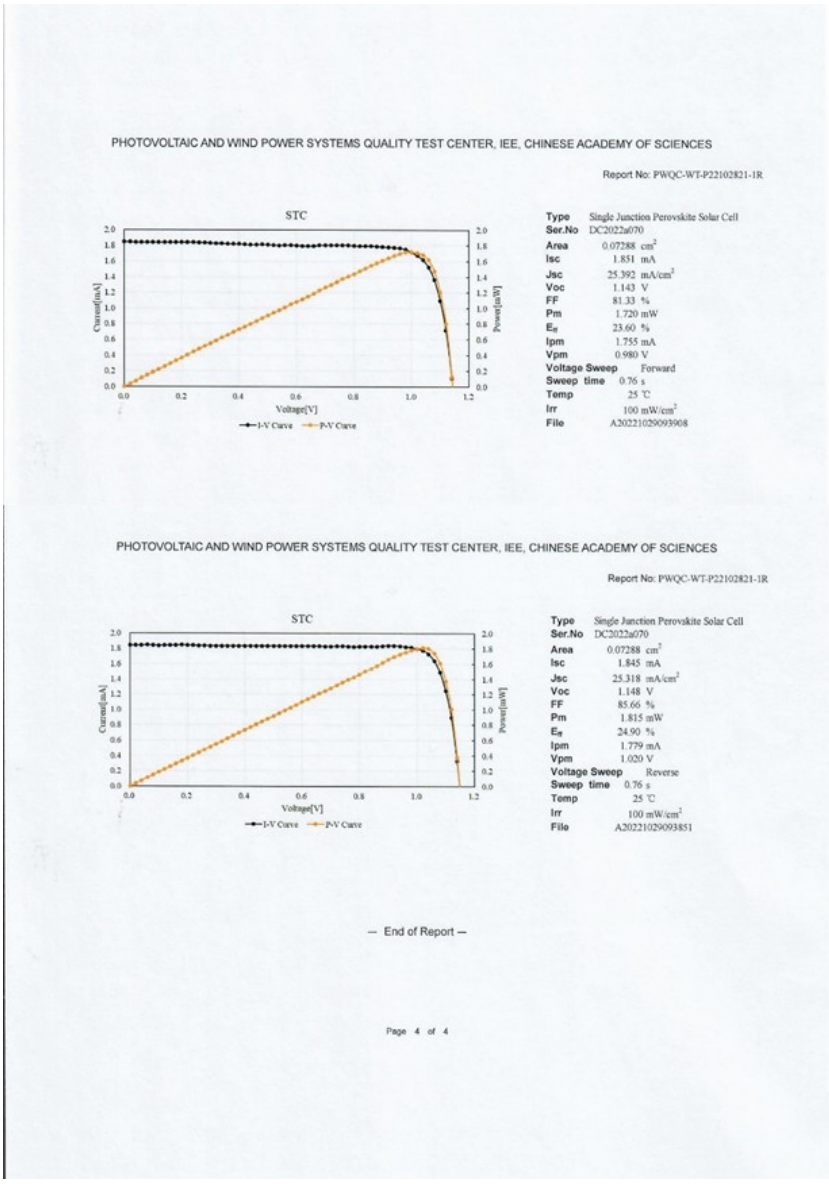

PHOTOVOLTAIC AND WIND POWER SYSTEMS QUALITY TEST CENTER, IEE, CHINESE ACADEMY OF SCIENCES

Report No: PWQC-WT-P22102821-1R

Type	Single Junction Perovskite Solar Cell
Ser.No	DC2022a070
Area	0.07288 cm^2
Isc	1.851 mA
Jsc	25.392 mA/cm^2
Voc	1.143 V
FF	81.33 %
Pm	1.720 mW
E_{ff}	23.60 %
Ipm	1.755 mA
Vpm	0.980 V
Voltage Sweep	Forward
Sweep time	0.76 s
Temp	25 ℃
Irr	100 mW/cm^2
File	A20221029093908

PHOTOVOLTAIC AND WIND POWER SYSTEMS QUALITY TEST CENTER, IEE, CHINESE ACADEMY OF SCIENCES

Report No: PWQC-WT-P22102821-1R

Type	Single Junction Perovskite Solar Cell
Ser.No	DC2022a070
Area	0.07288 cm^2
Isc	1.845 mA
Jsc	25.318 mA/cm^2
Voc	1.148 V
FF	85.66 %
Pm	1.815 mW
E_{ff}	24.90 %
Ipm	1.779 mA
Vpm	1.020 V
Voltage Sweep	Reverse
Sweep time	0.76 s
Temp	25 ℃
Irr	100 mW/cm^2
File	A20221029093851

— End of Report —

Page 4 of 4

Fig. S33 Certified performance of target PSCs from the Institute of Electrical Engineering, Chinese Academy of Sciences (IEE, CAS, Beijing, China). The certified PCE of the champion device is 24.90% under reverse scan with a mask of 0.07288 cm^2.

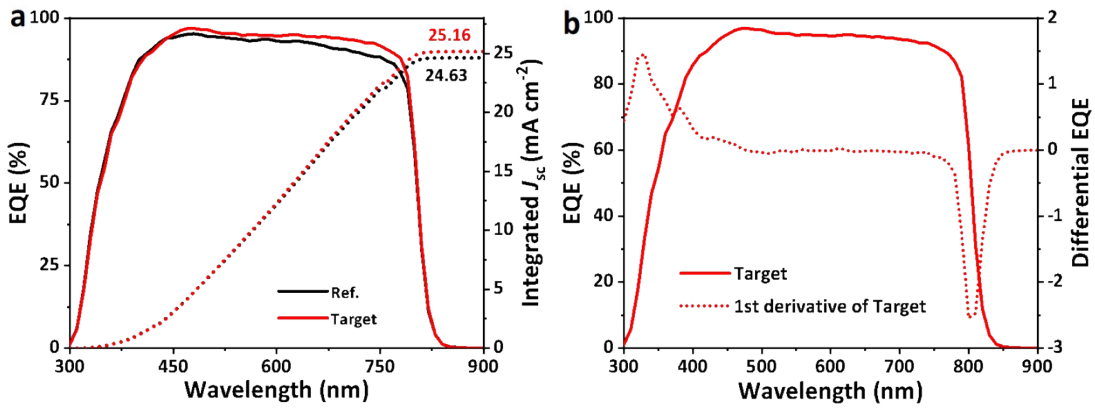

Fig. S34 (a) External quantum efficiency (EQE) spectra and integrated J_{SC} of reference and target devices. **(b)** Analysis of perovskite bandgap from the EQE derivative spectra.

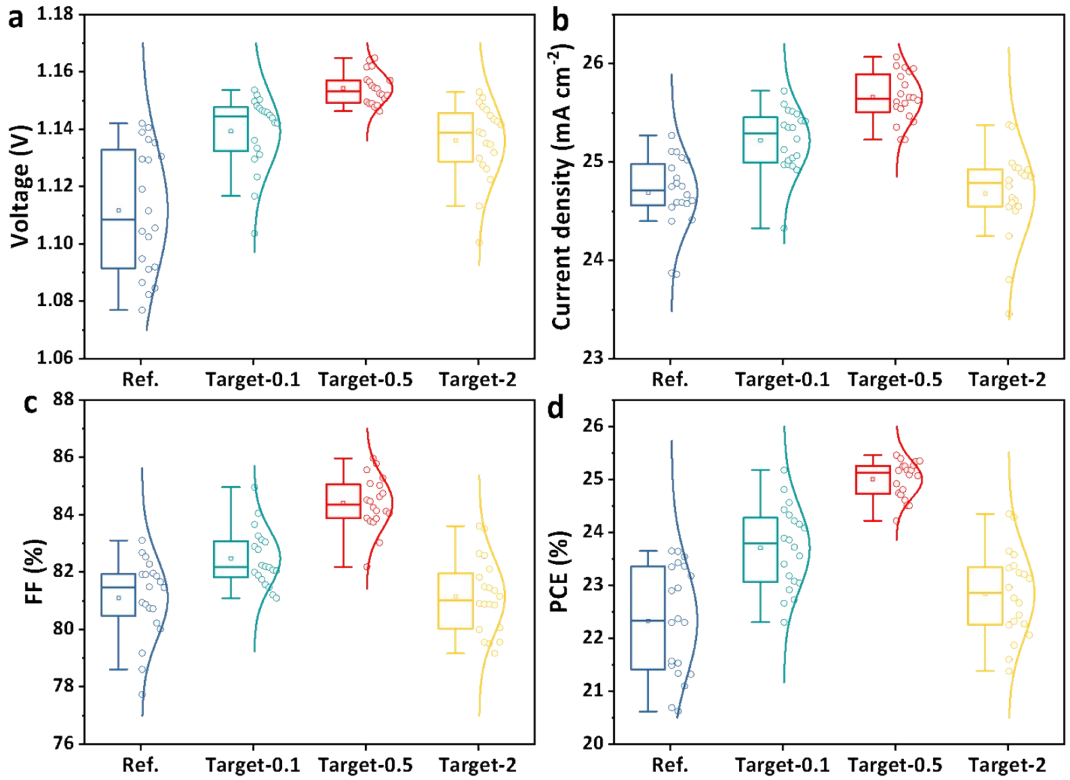

Fig. S35 The photovoltaic parameters of (**a**) *V*oc, (**b**) *J*sc, (**c**) FF, and (**d**) PCE for the devices with different concentrations of QA treatment (20 independent devices prepared at the same conditions for each type).

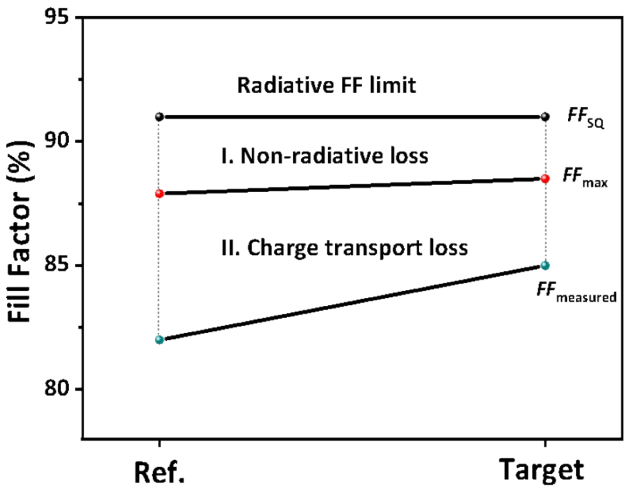

Fig. S36 The S-Q limit FF of reference and target devices includes non-radiative loss and charge transport loss. The green, red, and black pellets represent the value of $FF_{measured}$, the calculated FF_{max}, and FF_{SQ}, respectively.

Note: The deviation of the maximum FF (FF_{max}) with the SQ-limited FF (FF_{SQ}) and measured FF ($FF_{measured}$) stand for the non-radiative losses and charge transport losses, respectively. FF_{SQ} of the PSCs with a bandgap of 1.54 eV is ~0.901. In case of neglecting charge transport losses, the FF_{max} can be calculated by the equation of $FF_{max} = \frac{v_{oc} - ln(v_{oc} + 0.72)}{v_{oc} + 1}$, where $v_{oc} = \frac{qV_{oc}}{nk_BT}$, k_B is Boltzmann constant, q is the electron charge and T is the room temperature.[18,19] The FF_{max} of the reference and target devices were calculated to be ~0.879 and ~0.885, respectively. It can be observed that the target device exhibits the markedly cut-down gap between $FF_{measured}$ and FF_{max} compared to the reference one, indicating significantly restrained charge transport losses in the target devices.[20,21] That could be responsible for more efficient carrier charge extraction and transport.

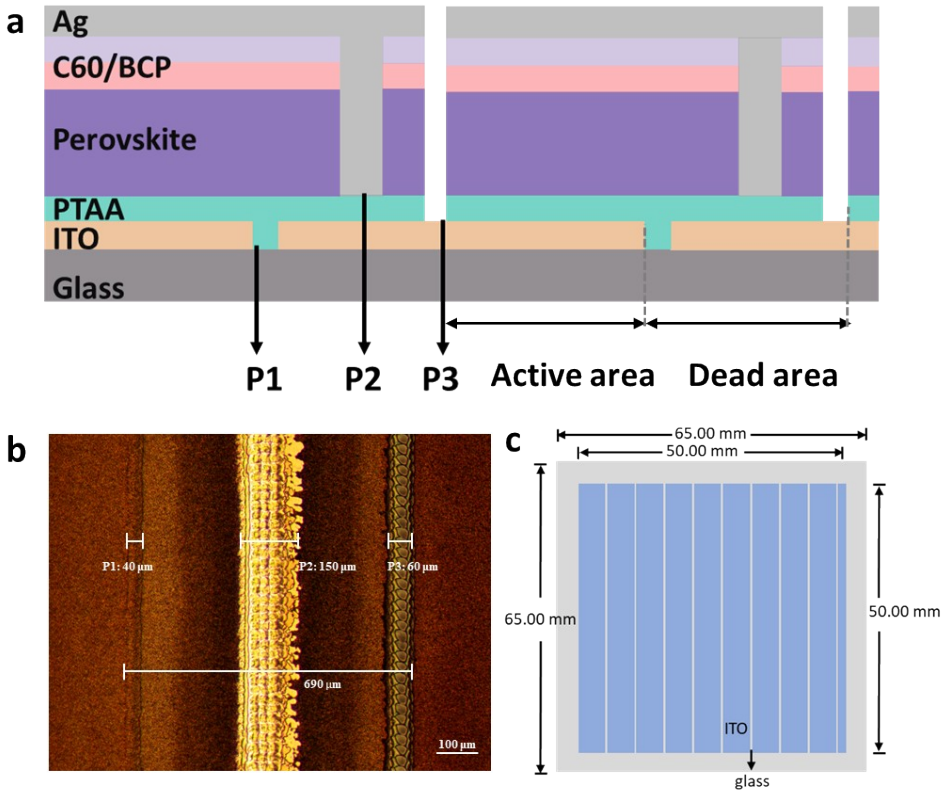

Fig. S37 (**a**) Side view of perovskite solar modules interconnected in series with nine sub-cells. (**b**) Optical photo of patterning for sub-cell separation in modules. The width of P1, P2, and P3 are 40, 150, and 60 µm, respectively. (**c**) Top view of the entire module, including the glass substrate, and ITO pattern.

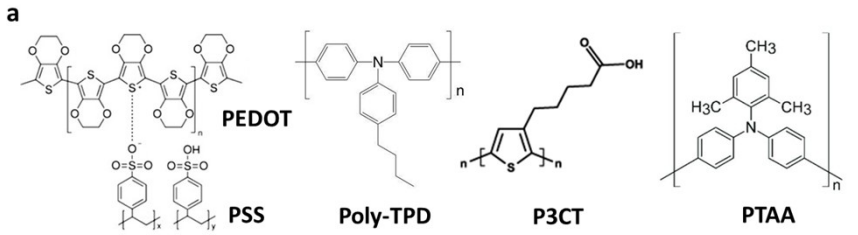

b

HTMs	HOMO (eV)	LUMO (eV)	Hole mobility ($cm^2 V^{-1} s^{-1}$)	References
PEDOT: PSS	-5.3	-2.2	0.045	*Adv. Mater.* 2013, 25, 2831.
Poly-TPD	-5.4	-2.4	10^{-4}	*Nat. Commun.* 2015, 6, 7747
P3CT	-5.1	-3.15	/	*ACS Appl. Mater. Interfaces* 2017, 9, 31357-31361
PTAA	-5.2~-5.1	-1.8~-1.7	3~6x10^{-4}	*Nat. Energy*, 2020, 5, 131-140

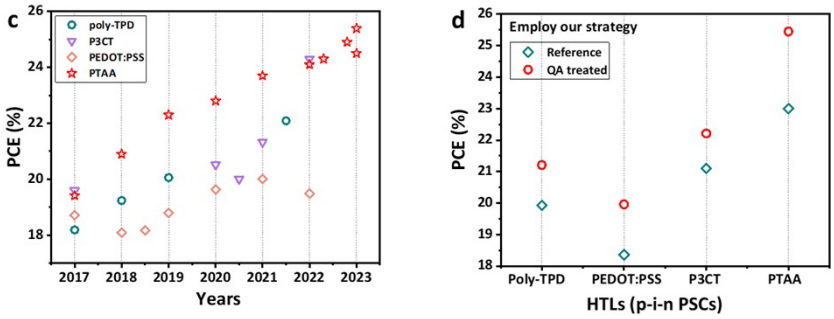

Fig. S38 (**a**) Molecular structure of typical organic HTMs: PEDOT: PSS,[22–25] poly-TPD,[26–29] P3CT,[30–32] and PTAA.[13,14,20,33–39] (**b**) Comparison of the physical properties of organic HTMs. (**c**) Review the recent efficiency of the state-of-the-art PSCs based on different HTMs. (**c**) Review the recent efficiency of the state-of-the-art PSCs based on different HTMs. (**d**) Comparison for the PCE of the p-i-n PSCs based on HTLs without (reference) and with QA treatment (QA treated).

Note: Typical organic materials, including poly-TPD, PEDOT: PSS, P3CT, and PTAA, exhibit different physical properties and have been widely employed in inverted PSCs (Fig. S38b). Additionally, we reviewed the photovoltaic performance of state-of-the-art inverted devices with different HTMs over the years in Fig. S38b. Here, we applied those HTMs in p-i-n devices as a platform to confirm the effectiveness and generality of our approach. After QA treatment, the efficiencies of all the devices were improved to varying degrees.

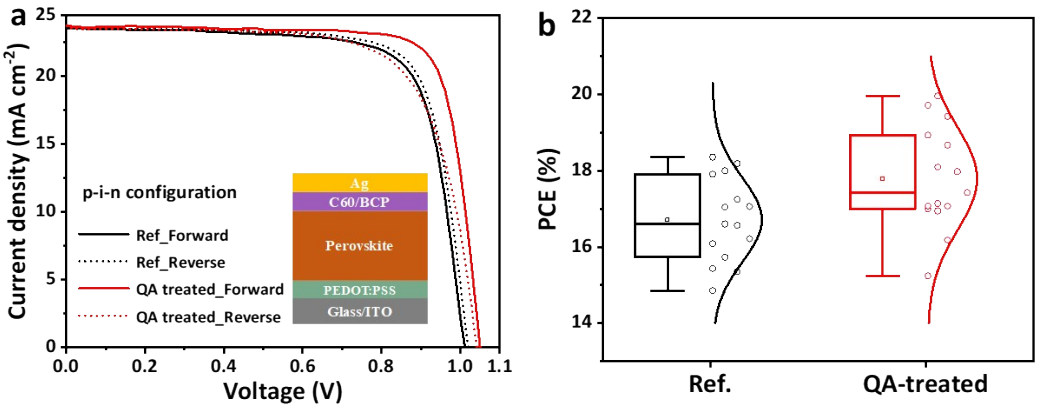

c

PEDOT: PSS as HTLs	Scan directions	V_{OC} (V)	J_{SC} (mA cm^{-2})	FF (%)	PCE (%)
Ref	Forward	1.01	23.65	74.79	17.91
	Reverse	1.02	23.66	76.12	18.36
QA-treated	Forward	1.04	23.88	80.33	19.96
	Reverse	1.05	23.74	77.92	19.72

Fig. S39 (**a**) *J-V* curves and (**b**) corresponding photovoltaic parameters of devices based on HTLs without (reference) and with QA treatment. The p-i-n device structure is ITO/PEDOT: PSS/$MAPbI_3$/C60/BCP/Ag.

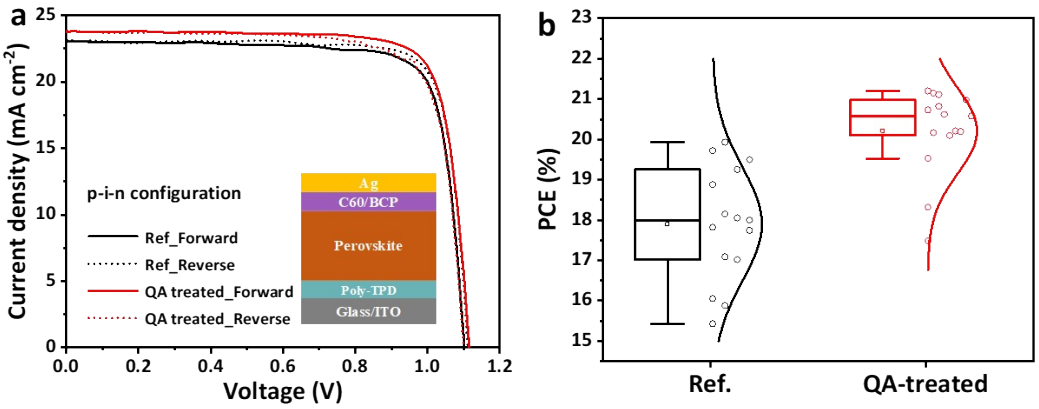

c

Poly-TPD as HTLs	Scan directions	*Voc* (V)	*Jsc* (mA cm^{-2})	FF (%)	PCE (%)
Ref	Forward	1.07	23.08	80.33	19.93
	Reverse	1.09	23.14	77.92	19.72
QA-treated	Forward	1.08	23.91	80.25	20.73
	Reverse	1.09	23.85	81.51	21.21

Fig. S40 (**a**) *J-V* curves and (**b**) corresponding photovoltaic parameters of devices based on HTLs without (reference) and with QA treatment. The p-i-n device structure is ITO/Poly-TPD/ Perovskite/C60/BCP/Ag.

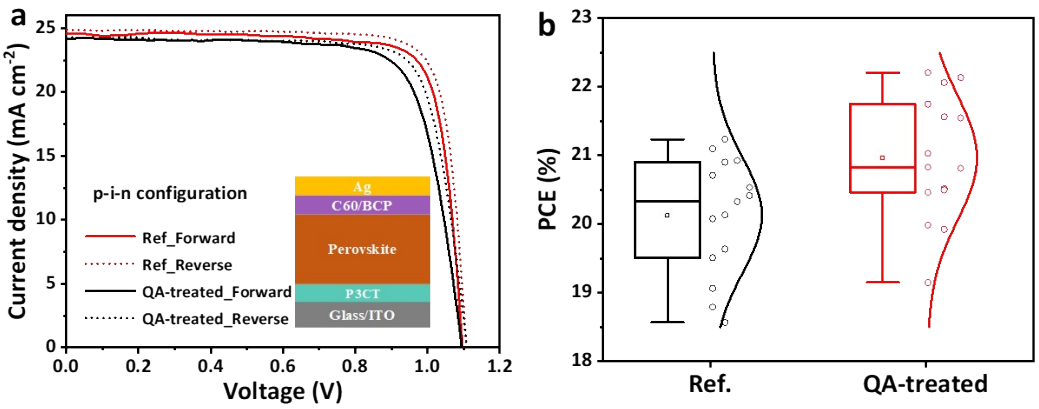

c

P3CT as HTLs	Scan directions	*Voc* (V)	*Jsc* (mA cm^{-2})	FF (%)	PCE (%)
Ref	Forward	1.09	24.25	75.96	20.08
	Reverse	1.10	24.34	78.62	21.10
QA-treated	Forward	1.09	24.49	81.04	21.75
	Reverse	1.11	24.53	81.90	22.21

Fig. S41 (**a**) *J-V* curves and (**b**) corresponding photovoltaic parameters of devices based on HTLs without (reference) and with QA treatment. The p-i-n device structure is ITO/P3CT-Na/ Perovskite/C60/BCP/Ag.

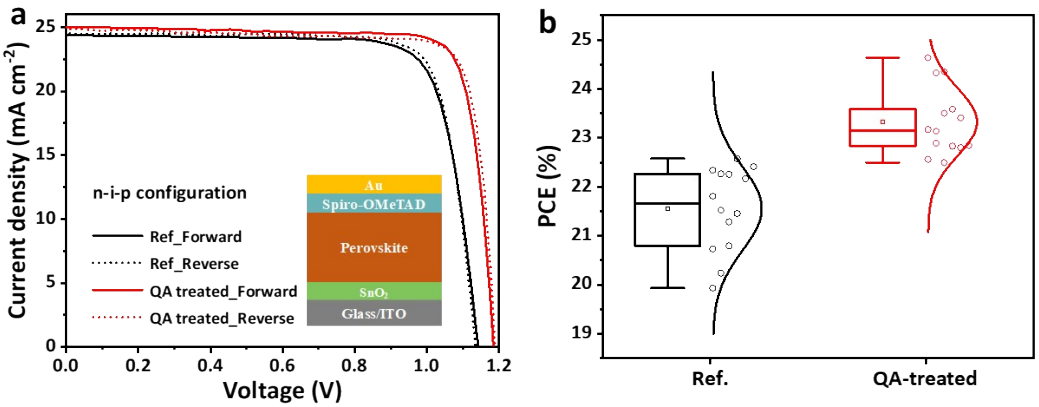

c

n-i-p devices	Scan directions	*Voc* (V)	*Jsc* (mA cm^{-2})	FF (%)	PCE (%)
Ref	Forward	1.14	24.25	78.79	21.81
	Reverse	1.13	24.50	80.37	22.34
QA-treated	Forward	1.17	24.94	83.20	24.64
	Reverse	1.18	24.85	83.07	24.33

Fig. S42 (**a**) *J-V* curves and (**b**) detailed photovoltaic parameters of n-i-p cells based on perovskite without (reference) and with QA treatment. The n-i-p device stack is ITO/SnO_2/$(Cs_{0.04}FA_{0.97}I_3)_{0.95}(MAPbBr_3)_{0.05}$/Spiro-OMeTAD/Au, where $(Cs_{0.04}FA_{0.97}I_3)_{0.95}(MAPbBr_3)_{0.05}$ perovskite has a bandgap of 1.55 eV (see our former work[40]).

Table S3 Mott-Schottky analysis of reference and target devices.

Samples	V_{fb} (V)	Slope (10^{15})	N_d (10^{10} cm^{-3})
Ref.	0.90	-1.12	1.08
Target	1.07	-3.05	0.395

Note: Calculate the flat-band voltage (V_{fb}) at the intersection of the Mott-Schottky curves and X= 0. The carrier density can be calculated from the slope of the curves based on the relationship, $slope = \frac{2}{\varepsilon_0 \varepsilon_r A^2 q N_d}$. The carrier concentration can be derived by the slope of the Mott-Schottky curves through the equation of $N_d = \frac{2}{\varepsilon_0 \varepsilon_r A^2 q k}$, where k is the slope, A is an active area of the device, q is the elementary charge, ε_0 and ε_r is the vacuum dielectric constant and dielectric constant of perovskite, respectively.[41]

Table S4 Statistic of corresponding parameters by Hall effect measurements.

Samples	Carrier density (10^{20} cm^{-3})	Conductivity (10^3 S cm^{-1})	Hall mobility (cm^2 V^{-1} s^{-1})
Ref.	5.02	2.06	26.4
QA-0.1	4.59	2.10	28.6
QA-0.5	4.44	2.22	31.1
QA-2.0	4.14	2.12	31.3

Note: The Hall effect was conducted with a four-probe arrangement, where metal electrodes are made at the four corners of the sample and contacted with metal probes. The samples were probed in a magnetic field environment with setting the appropriate current and thickness. The obtained results were analyzed using the instrument software, employing the Vander-burg principle as the underlying methodology. This analytical process is impacted by factors, such as magnetic field current, Hall current, and samples as pre-treatment conducted prior to testing. It is important to emphasize that the reliability of the results presented here is contingent on their comparison between reference and target samples.

Table S5 Vertical transit mobility calculation through a combination TPC measurement with Mott-Schottky analysis.

Sample	L (nm)	V_{bi} (V)	τ_t (μs)	μ_t (10^{-3}cm^2 V^{-1}s^{-1})
Ref.	728	0.90	2.69	2.18
Target	789.3	1.07	1.92	3.03

Note: The vertical transit mobility μ_t is determined by $\mu_t = \frac{L^2}{\tau_t V_{bi}}$, where L is the thickness of the devices, τ_t is the transit time extracted from the transit photocurrent decay curve and V_{bi} is the built-in potential extracted from the Mott-Schottky analysis.[42]

Table S6 The corresponding fitting parameters from TRPL spectra.

Samples	A_1	A_2	τ_1 (ns)	τ_2 (ns)	τ_{avg} (ns)
Ref.	0.144	0.317	104	677	640
Target	8.25	0.454	94	497	184

Note: The average lifetime was calculated using the equation $\tau_{avg} = \frac{A_1\tau_1^2 + A_2\tau_2^2}{A_1\tau_1 + A_2\tau_2}$.

Table S7 Summarized corresponding parameters for the space-charge-limited current (SCLC) measurements of hole-only inverted devices (V_{TEL}, onset trap-filling voltage).

Samples	V_{TEL} (V)	N_t (10^{15} cm^{-3})	μ (10^{-3} cm^2 V^{-1}s^{-1})
Ref.	0.66	5.84	1.2
Target	0.43	2.15	2.2

Note: All devices featuring the ITO/PTAA (QA)/PVSK/PTAA/Ag architecture were uniformly fabricated under identical conditions. This stringent consistency was maintained to ensure accurate testing across all devices. The trap density (N_t) was calculated by the function of $Nt = \frac{2\varepsilon_0\varepsilon_r V_{TEL}}{eL^2}$, where ε_r is the relative dielectric constant, ε_0 is vacuum permittivity (8.854×10^{-12} F/m), e is electron charge (1.6×10^{-19} C), and L is the thickness of perovskite layer.[23,24] The trap-free space-charge limited region at high bias can be fitted according to the relation of $I \propto V^n$, where n corresponds to the exponent of the dependence of V. The carrier mobility (μ) can be calculated according to Mott-Gurney's law: $\mu = \frac{8J_D L^3}{9\varepsilon_0\varepsilon_r V^2}$, where J_D is the current density.

Table S8 The photovoltaic parameters of reference and target devices with QA treatment in different concentrations.

Samples	V_{OC} (V)	J_{SC} (mA cm^{-2})	FF (%)	PCE (%)
Ref.	1.13	24.97	82.23	23.52
Target -0.1	1.14	25.51	82.60	24.32
Target -0.5	1.16	25.61	85.66	25.45
Target -2.0	1.14	24.87	82.53	23.72

Table S9 Statistics of the Shockley-Queisser limited FF (FF_{SQ}), the calculated maximum FF (FF_{max}), and measured FF ($FF_{measured}$) of the inverted devices with a bandgap of 1.54 eV.

Samples	$\mathbf{FF_{SQ}}$	$\mathbf{FF_{max}}$	$\mathbf{FF_{measured}}$	$\boldsymbol{R_s}$ **(ohm)**	$\boldsymbol{R_{sh}}$ **(ohm)**
Ref.	0.91	0.879	0.820	11.38	65654.7
Target	0.91	0.885	0.866	9.32	75855.1

Table S10 Comparison of the reported interfacial additives of the PTAA layer in inverted PSCs.[13,43–46]

Passivators for PTAA layer	Polyelectrolyte PFN-Br	1,4butanediammonium iodide (BDAI)	[2-(9H-carbazol-9-yl) ethyl] phosphonic acid	3-(1-pyridinio)-1-propanesulfonate (PPS)	4-fluorophenylethylammonium iodide (F-PEAI)	QA (SA/TA)
Molecule Structure	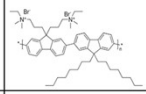	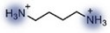			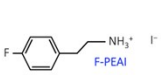	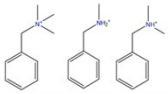
Hole mobility ($cm^2 V^{-1} s^{-1}$)	/	/	/	/	/	31.3 (Hall mobility)
Conductivity (10^3 S cm^{-1})	/	/	/	/	/	2.22
Energy level match (eV)	√	√	√	√	/	√
Wettability	/	√	/	/	√	√
Stability (MPPT /SPO)	500 h (85 °C in N_2)	SPO for 10 h	SPO for 600 s	100 h (T80; 20-30 ℃, RH20-30%)	35 h (T99; N_2)	3000 h (T99; N_2)
PCE	20.6%	22.31%	22.17%	21.7%	23.7%	25.45% (certified 24.9%)
Price ($/g, Sigma)	4300	13	416	648	9	5
Reference	Adv. Mater. 2023, 35, 2206345	Joule 2020, 4, 1248–1262,	Small 2022, 18, 2201694	ACS Energy Lett. 2021, 6, 1596–1606	Sci. Adv. 2021, 7, eabj7930	**In this work**

Note: Regarding the previously reported interfacial additive, such as PFN-Br, PEAI, and PSS (listed in Table S10), the similarities between QA and those ammonium salts are just in the typical chemical nature of ammonium. Every chemical compound should be individual and unique, rather than simply confusing them as their similar functional groups.

Table S11 Summary table for photovoltaic parameters of reported state-of-the-art perovskite solar cells in the n-i-p[12,21,47–54] and p-i-n[13,14,20,32,33,55–57] configurations.

Years	Configurations	V_{OC} (V)	J_{SC} (mA cm^{-2})	*FF* (%)	PCE (%)	References
2017	n-i-p	1.11	23.62	80.3	22.1	*Science* 356, aan2301
2018	n-i-p	1.13	24.91	80.5	22.6	*Nat. Energy* 3, 682-689
2019	n-i-p	1.14	24.92	79.6	22.7	*Nature* 567, 511-515
2019	n-i-p	1.18	25.2	78.4	23.3	*Nat. Photonics* 13, 460-466
2019	n-i-p	1.15	26.1	79.0	23.7	*Science* 366, aay7044
2020	n-i-p	1.18	26.2	79.6	24.6	*Science* 369, abb7167
2021	n-i-p	1.18	25.1	84.8	25.2	*Nature* 590, 587-593
2021	n-i-p	1.17	26.1	81.8	25.2	*Nature* 592, 381-385
2021	n-i-p	1.18	25.7	83.2	25.5	*Nature* 598, 444-450
2022	n-i-p	1.18	23.13	86.6	23.3	*Nature* 601, 573-578
2022	n-i-p	1.128	25.64	85.2	24.66	*Energy Environ. Sci.,* 15, 4813–4822
2022	n-i-p	1.18	26.2	82.6	25.6	*Science* 377, abp8873
2023	n-i-p	1.18	25.64	85.1	25.7	*Nature (2023)*
2019	p-i-n#	1.14	23.8	82	22.3	*Nat. Energy* 5, 131-140
2020	p-i-n#	1.21	22.59	81.6	23.8	*Joule* 4, 1248–1262
2020	p-i-n#	1.16	24.7	79.2	22.8	*J. Am. Chem. Soc* 142, 20134-20142
2021	p-i-n#	1.18	24.1	85	23.7	*Sci. Adv.* 7, eabj7930
2021	p-i-n#	1.17	24.1	84.2	23.8	*Science* 373, 902–907
2022	p-i-n	1.14	25.3	81.3	23.5	*Science* 375, abl5676
2022	p-i-n#	1.18	25.6	80.6	24.3	*Science* 376, abm8566
2022	p-i-n	1.16	25.4	81.5	24.1	*Nature* 611, 278-283
2023	p-i-n#	1.17	25.5	82.5	24.6	*Science* 380, 823–829

2023	p-i-n	1.16	25.73	82.5	24.5	*Science* 379, 690–694
2023	p-i-n	1.17	25.05	82.7	24.9	*Science* 379, 683-690
2023	p-i-n	1.189	25.54	83.2	25.39	*Nature*
2023	**p-i-n#**	**1.14**	**25.3**	**85.6**	**24.9**	**This work**

Note: The symbol of p-i-n# represents the PSCs in the p-i-n configuration employing PTAA as HTMs.

References

1 W. Shockley and H. J. Queisser, *J. Appl. Phys.*, 1961, **32**, 510–519.

2 J.-F. Guillemoles, T. Kirchartz, D. Cahen and U. Rau, *ArXiv Prepr. ArXiv*, 2019, **1903**, 11954.

3 J.-F. Guillemoles, T. Kirchartz, D. Cahen and U. Rau, *Nat. Photonics*, 2019, **13**, 501–505.

4 J. F. Guillemoles, *Photoniques*, 2021, **110**, 48–52.

5 Y. Yuan, G. Yan, R. Hong, Z. Liang and T. Kirchartz, *Adv. Mater.*, 2022, **34**, 2108132.

6 L. Krückemeier, U. Rau, M. Stolterfoht and T. Kirchartz, *Adv. Energy Mater.*, 2020, **10**, 1902573.

7 M. A. Green, *Sol. Cells*, 1982, **7**, 337–340.

8 M. A. Green, *Solid State Electron.*, 1981, **24**, 788–789.

9 U. Rau, B. Blank, T. C. M. Müller and T. Kirchartz, *Phys. Rev. Appl.*, 2017, **7**, 044016.

10 E. H. Jung, N. J. Jeon, E. Y. Park, C. S. Moon, T. J. Shin, T.-Y. Yang, J. H. Noh and J. Seo, *Nature*, 2019, **567**, 511–515.

11 Q. Jiang, Y. Zhao, X. Zhang, X. Yang, Y. Chen, Z. Chu, Q. Ye, X. Li, Z. Yin and J. You, *Nat. Photonics*, 2019, **13**, 460–466.

12 J. You, Y. Zhao, F. Ma, Z. Qu, S. Yu, T. Shen, H.-X. Deng, X. Chu, X. Peng, Y. Yuan and X. Zhang, *Science*, 2022, **377**, 531–534.

13 M. Degani, Q. An, M. Albaladejo-Siguan, Y. J. Hofstetter, C. Cho, F. Paulus, G. Grancini and Y. Vaynzof, *Sci. Adv.*, 2021, **7**, eabj7930.

14 Z. Zhu, Z. Li, B. Li, X. Wu, S. A. Sheppard, S. Zhang, D. Gao and N. J. Long, *Science*, 2022, **376**, 416–420.

15 L. Yin, C. Ding, C. Liu, C. Zhao, W. Zha, I. Z. Mitrovic, E. G. Lim, Y. Han, X. Gao, L. Zhang, H. Wang, Y. Li, S. Wilken, R. Österbacka, H. Lin, C.-Q. Ma and C. Zhao, *Adv. Energy Mater.*, **n/a**, 2301161.

16 Z. Liang, H. Xu, Y. Zhang, G. Liu, S. Chu, Y. Tao, X. Xu, S. Xu, L. Zhang and X. Chen, *Adv. Mater.*, 2022, 2110241.

17 J. Zhao, Y. Deng, H. Wei, X. Zheng, Z. Yu, Y. Shao, J. E. Shield and J. Huang, *Sci. Adv.*, 2017, **3**, eaao5616.

18 J. Wang, J. Zhang, Y. Zhou, H. Liu, Q. Xue, X. Li, C.-C. Chueh, H.-L. Yip, Z. Zhu and A. K. Y. Jen, *Nat. Commun.*, 2020, **11**, 177.

19 M. A. Green, *Sol. Cells*, 1982, **7**, 337–340.

20 J. Xu, W. Peng, K. Mao, F. Cai, H. Meng, Z. Zhu, T. Li, S. Yuan, Z. Xu, X. Feng, J. Xu and M. D. McGehee, *Science*, 2023, **379**, 683–690.

21 X. Li, X. Wu, B. Li, Z. Cen, Y. Shang, W. Lian, R. Cao, L. Jia, Z. Li, D. Gao, X. Jiang, T. Chen, Y. Lu, Z. Zhu and S. Yang, *Energy Environ. Sci.*, 2022, **15**, 4813–4822.

22 K. Chen, Q. Hu, T. Liu, L. Zhao, D. Luo, J. Wu, Y. Zhang, W. Zhang, F. Liu, T. P. Russell, R. Zhu and Q. Gong, *Adv. Mater.*, 2016, **28**, 10718–10724.

23 C. Xu, Y. Yao, G. Wang, J. Dong, G. Xu, Y. Zhong, D. Lu, X. Zhao, D. Liu, G. Zhou, X. Yang, P. Li, L. Chen and Q. Song, *Chem. Eng. J.*, 2022, **428**, 132074.

24 S. Hu, K. Otsuka, R. Murdey, T. Nakamura, M. A. Truong, T. Yamada, T. Handa, K. Matsuda, K. Nakano, A. Sato, K. Marumoto, K. Tajima, Y. Kanemitsu and A. Wakamiya, *Energy Environ. Sci.*, 2022, **15**, 2096–2107.
25 K. M. Reza, A. Gurung, B. Bahrami, S. Mabrouk, H. Elbohy, R. Pathak, K. Chen, A. H. Chowdhury, M. T. Rahman, S. Letourneau, H.-C. Yang, G. Saianand, J. W. Elam, S. B. Darling and Q. Qiao, *J. Energy Chem.*, 2020, **44**, 41–50.
26 J. Zhang, B. Yu, Y. Sun and H. Yu, *Adv. Energy Mater.*, 2023, **13**, 2300382.
27 X. Hu, C. Tao, J. Liang, C. Chen, X. Zheng, J. Li, J. Li, Y. Liu and G. Fang, *Sol. Energy*, 2021, **218**, 368–374.
28 F. Zhang, Y. Hou, S. Wang, H. Zhang, F. Zhou, Y. Hao, S. Ye, H. Cai, J. Song and J. Qu, *Sol. RRL*, 2021, **5**, 2100190.
29 X. Xu, C. Ma, Y. Cheng, Y.-M. Xie, X. Yi, B. Gautam, S. Chen, H.-W. Li, C.-S. Lee, F. So and S.-W. Tsang, *J. Power Sources*, 2017, **360**, 157–165.
30 Q. Liao, Y. Wang, X. Yao, M. Su, B. Li, H. Sun, J. Huang and X. Guo, *ACS Appl. Mater. Interfaces*, 2021, **13**, 16744–16753.
31 S. Li, B. He, J. Xu, H. Lu, J. Jiang, J. Zhu, Z. Kan, L. Zhu and F. Wu, *Nanoscale*, 2020, **12**, 3686–3691.
32 J. Fang, X. Li, W. Zhang, X. Guo, C. Lu and J. Wei, *Science*, 2022, **375**, 434–437.
33 S. Chen, X. Dai, S. Xu, H. Jiao, L. Zhao and J. Huang, *Science*, 2021, **373**, 902–907.
34 C. Fei, N. Li, M. Wang, X. Wang, H. Gu, B. Chen, Z. Zhang, Z. Ni, H. Jiao, W. Xu, Z. Shi, Y. Yan and J. Huang, *Science*, 2023, **380**, 823–829.
35 X. Wu, D. Gao, X. Sun, S. Zhang, Q. Wang, B. Li, Z. Li, M. Qin, X. Jiang, C. Zhang, Z. Li, X. Lu, N. Li, S. Xiao, X. Zhong, S. Yang, Z. Li and Z. Zhu, *Adv. Mater.*, **n/a**, 2208431.
36 Y. Xu, S. Xiong, S. Jiang, J. Yang, D. Li, H. Wu, X. You, Y. Zhang, Z. Ma, J. Xu, J. Tang, Y. Yao, Z. Sun and Q. Bao, *Adv. Energy Mater.*, **n/a**, 2203505.
37 X. Xu, X. Ji, R. Chen, F. Ye, S. Liu, S. Zhang, W. Chen, Y. Wu and W.-H. Zhu, *Adv. Funct. Mater.*, 2022, **32**, 2109968.
38 D. Luo, W. Yang, Z. Wang, A. Sadhanala, Q. Hu, R. Su, R. Shivanna, G. F. Trindade, J. F. Watts, Z. Xu, T. Liu, K. Chen, F. Ye, P. Wu, L. Zhao, J. Wu, Y. Tu, Y. Zhang, X. Yang, W. Zhang, R. H. Friend, Q. Gong, H. J. Snaith and R. Zhu, .
39 C. M. Wolff, F. Zu, A. Paulke, L. P. Toro, N. Koch and D. Neher, *Adv. Mater.*, 2017, **29**, 1700159.
40 G. Liu, H. Zheng, J. Ye, S. Xu, L. Zhang, H. Xu, Z. Liang, X. Chen and X. Pan, *ACS Energy Lett.*, 2021, **6**, 4395–4404.
41 O. Almora, C. Aranda, E. Mas-Marzá and G. Garcia-Belmonte, *Appl. Phys. Lett.*, 2016, **109**, 173903.
42 J. Huang, Y. Shao, Z. Xiao, C. Bi and Y. Yuan, *Nat. Commun.*, 2014, **5**, 5784.
43 S. Wu, J. Zhang, Z. Li, D. Liu, M. Qin, S. H. Cheung, X. Lu, D. Lei, S. K. So, Z. Zhu and Alex. K.-Y. Jen, *Joule*, 2020, **4**, 1248–1262.
44 Y. Huang, T. Liu, D. Li, Q. Lian, Y. Wang, G. Wang, G. Mi, Y. Zhou, A. Amini, B. Xu, Z. Tang, C. Cheng and G. Xing, *Small*, 2022, **18**, 2201694.
45 Q. Zhou, J. Qiu, Y. Wang, M. Yu, J. Liu and X. Zhang, *ACS Energy Lett.*, 2021,

1596–1606.
46 P. Chen, Y. Xiao, L. Li, L. Zhao, M. Yu, S. Li, J. Hu, B. Liu, Y. Yang, D. Luo, C.-H. Hou, X. Guo, J.-J. Shyue, Z.-H. Lu, Q. Gong, H. J. Snaith and R. Zhu, *Adv. Mater.*, 2023, **35**, 2206345.
47 E. H. Jung, N. J. Jeon, E. Y. Park, C. S. Moon, T. J. Shin, T.-Y. Yang, J. H. Noh and J. Seo, *Nature*, 2019, **567**, 511–515.
48 N. J. Jeon, H. Na, E. H. Jung, T.-Y. Yang, Y. G. Lee, G. Kim, H.-W. Shin, S. Il Seok, J. Lee and J. Seo, *Nat. Energy*, 2018, **3**, 682–689.
49 J. J. Yoo, G. Seo, M. R. Chua, T. G. Park, Y. Lu, F. Rotermund, Y.-K. Kim, C. S. Moon, N. J. Jeon and J.-P. Correa-Baena, *Nature*, 2021, **590**, 587–593.
50 Q. Jiang, Y. Zhao, X. Zhang, X. Yang, Y. Chen, Z. Chu, Q. Ye, X. Li, Z. Yin and J. You, *Nat. Photonics*, 2019, **13**, 460–466.
51 M. Jeong, I. W. Choi, E. M. Go, Y. Cho, M. Kim, B. Lee, S. Jeong, Y. Jo, H. W. Choi, J. Lee, J.-H. Bae, S. K. Kwak, D. S. Kim and C. Yang, *Science*, 2020, **369**, 1615–1620.
52 H. Min, M. Kim, S.-U. Lee, H. Kim, G. Kim, K. Choi, J. H. Lee and S. I. Seok, *Science*, 2019, **366**, 749–753.
53 W. S. Yang, B.-W. Park, E. H. Jung, N. J. Jeon, Y. C. Kim, D. U. Lee, S. S. Shin, J. Seo, E. K. Kim, J. H. Noh and S. I. Seok, *Science*, 2017, **356**, 1376–1379.
54 J. Peng, *Nature*.
55 Q. Jiang, J. Tong, Y. Xian, R. A. Kerner, S. P. Dunfield, C. Xiao, R. A. Scheidt, D. Kuciauskas, X. Wang, M. P. Hautzinger, R. Tirawat, M. C. Beard, D. P. Fenning, J. J. Berry, B. W. Larson, Y. Yan and K. Zhu, *Nature*, 2022, **611**, 278–283.
56 X. Zheng, Y. Hou, C. Bao, J. Yin, F. Yuan, Z. Huang, K. Song, J. Liu, J. Troughton, N. Gasparini, C. Zhou, Y. Lin, D.-J. Xue, B. Chen, A. K. Johnston, N. Wei, M. N. Hedhili, M. Wei, A. Y. Alsalloum, P. Maity, B. Turedi, C. Yang, D. Baran, T. D. Anthopoulos, Y. Han, Z.-H. Lu, O. F. Mohammed, F. Gao, E. H. Sargent and O. M. Bakr, *Nat. Energy*, 2020, **5**, 131–140.
57 Q. Tan, Z. Li, G. Luo, X. Zhang, B. Che, G. Chen, H. Gao, D. He, G. Ma, J. Wang and J. Xiu, *Nature*, , DOI:https://doi.org/ 10.1038/s41586-023-06207-0.